Direct Aeroacoustic Simulations Based on High Order Discontinuous Galerkin Schemes

Andrea Beck and Claus-Dieter Munz

Abstract In this chapter, we discuss some of the challenges that arise for the direct numerical computation of noise generation and transport. Noise sources are associated with the non-linearities of the underlying hydrodynamics, i.e. with the turbulent fluctuations across the energy spectrum. Thus, the numerical resolution of these sound sources not only inherits the numerical difficulties that arise for general DNS and LES of turbulent flows, but the scale separation between the hydrodynamic velocity fluctuations and the radiated pressure waves adds additional challenges, for example in terms of boundary conditions and numerical approximation accuracy. Therefore, a highly efficient and accurate numerical scheme is necessary. The framework presented herein is based on a particular version of the Discontinuous Galerkin method, in which a nodal as well as discretely orthogonal basis is used for computational efficiency. This discretization choice allows arbitrary order in space while also supporting unstructured meshes. After discussing the details of the framework, examples of direct noise computation are presented, with a special focus on the numerical simulation of acoustic feedback in a complex automotive application.

1 Introduction

The field of aeroacoustics encompasses the sound waves generated by and propagated through unsteady turbulent or vortical aerodynamic internal and external flows. Computational methods that are aimed at simulating these sound waves or their effects are often termed Computational Aeroacoustics (CAA) methods, which are a subset of the more general Computational Fluids Dynamics (CFD) field. The main challenge in the numerical approximation of aeroacoustics stems from its multiscale nature. The generating mechanism is inherently non-linear and unsteady, which precludes - without strong assumptions - time-averaged simulation schemes like the Reynolds-averaged Navier–Stokes (RANS) approach. Different theoretical

A. Beck (✉) · C.-D. Munz
Numerics Research Group, Institute of Aerodynamics and Gasdynamics,
Pfaffenwaldring 21, 70569 Stuttgart, Germany
e-mail: beck@iag.uni-stuttgart.de
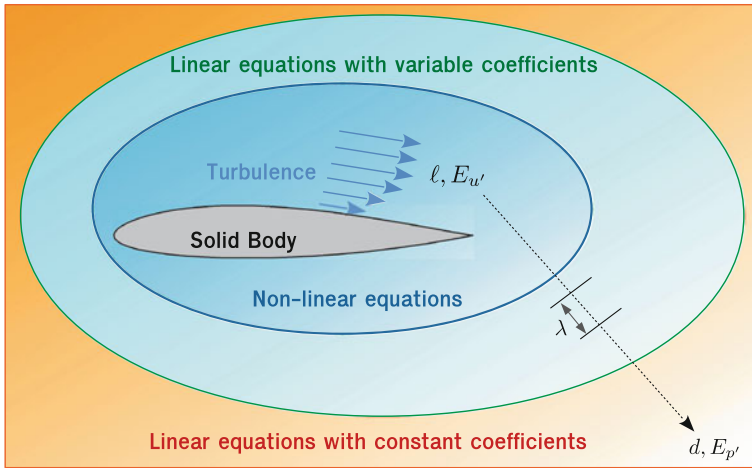
Fig. 1 Equations regimes and scales for aeroacoustics

interpretations regarding the source of sound generation exist, with the classical one focusing on the role of velocity fluctuations (Lighthill 1952) and a more recent one emphasizing vortical structures as the source mechanism for sound waves (Howe 2003). From both points of view however, it is clear that a successful simulation of aeroacoustics must include an accurate resolution of these generating mechanisms.

From a *physical* point of view, aeroacoustic problems can be categorized into those governed by non-linear effects, i.e. mainly the generation of pressure fluctuations from non-linear hydrodynamics, and those that are essentially linear, e.g. radiation into the far field, refraction or scattering. In Fig. 1, the relevant sets of equations (and thus the applicable numerical approaches discussed below) and the relevant scales are shown for a typical CAA problem.

Along a solid body, a turbulent boundary layer develops and radiates noise into its surroundings. It interacts with the trailing edge and thereby produces sound through the enhanced non-linearities in that region. A typical characteristic length of this generation mechanism is the boundary layer thickness ℓ. The energy content of the velocity fluctuations is characterized by $E_{u'}$. Since the relevant processes for the sound generation are inherently unsteady and non-linear, the full compressible Navier–Stokes equations are necessary to describe these processes accurately. As the time scale of the sound waves matches that of its source, the resulting wave length of the radiated sound is directly proportional to the speed of sound c, which explains the large discrepancy between λ and ℓ for low Mach number flows. For increasing Mach numbers, this clear scale separation vanishes. Further away from the solid body, the influence of non-linearities and viscosity is reduced and thus acoustic source terms vanish. Here, Euler equations and their linearized version (LEE) can be used to simulate acoustic transport by a background flow field, in which source terms generate the sound waves. Since the characteristic length ℓ now no longer needs to be resolved, the acoustic wave lengths λ and the associated wave speed

c now determine the spatial and temporal resolution requirements. This so-called hybrid approach, which is discussed in more detail below, thus explicitly exploits the scale separation. Even further away from the sound source, when $d/\lambda \gg 1$ and thus the source region becomes acoustically compact and reflections or diffraction are negligible, integral approaches based on the wave equation can be used to propagate the sound through the far field.

An example that clearly highlights the difficulties arising from the scale separation between the hydrodynamic source and the acoustic waves is given in a review by Lele: For a supersonic jet, the ratio of $E_{p'}/E_{u'}$ is only about 0.01, while for most other noise generation mechanisms, this ratio is even considerably smaller (Lele 1997).

From a *computational* point of view, the CAA methods (based on the equations discussed in Fig. 1) can be classified into two broad categories: The *direct* approach, labeled Direct Noise Computation (DNC) and the indirect or *hybrid* approach.

The direct approach is based on first principles and avoids any modeling approximations. It does not introduce an a priori conceptual split into a flow or hydrodynamic part and an acoustic part, but solves the full compressible flow equations which contain the sound generation mechanisms through non-linear vortical interactions. The solution to this single set of equations then contains all the physical effects included in the equations together with their coupling. In particular, acoustic feedback onto the flow field is naturally included in this approach.

For a meaningful DNC, numerical schemes must thus capture the unsteady solution over a wide range of local flow scales (to account for the non-linear source effects) and across large spatial and temporal scales (to account for the typically large length scales of the acoustic waves compared to the hydrodynamics). It therefore mandates numerical schemes that are capable of high local resolution as well as efficient and accurate long-term wave transport. While Direct Numerical Simulation (DNS), which resolves all flow scales including the dissipation range, is the preferred method of choice, it is essentially restricted by the direct dependency of its cost on the flow Reynolds number *Re*. Resolving only the dynamically important scales and modeling the isotropic parts by a subgrid scale model in a Large Eddy Simulation (LES) ameliorates this restriction and expands the range of applicability of DNC, but introduces the additional complexity of subgrid closure.

Another important conceptual complexity in DNC which should not be overlooked is the postprocessing of the solution, i.e. the a posteriori identification of acoustic sources and acoustic transport from the compressible flow field.

In the hybrid approach, the computation of the flow is decoupled from the computation of the sound. CAA then becomes a two-step, forward-coupled simulation approach. This separation is motivated by the disparity between the large length scales and low energy content of the acoustic field compared to the hydrodynamic field, i.e. the fundamental assumption states that while the unsteady vortical flow field generates sound waves and influences their propagation, these waves do not influence the flow field and act as a passive sink for the acoustic energy. This presumption is a good approximation in low Mach number flows, with the exception of acoustic feedback mechanisms.
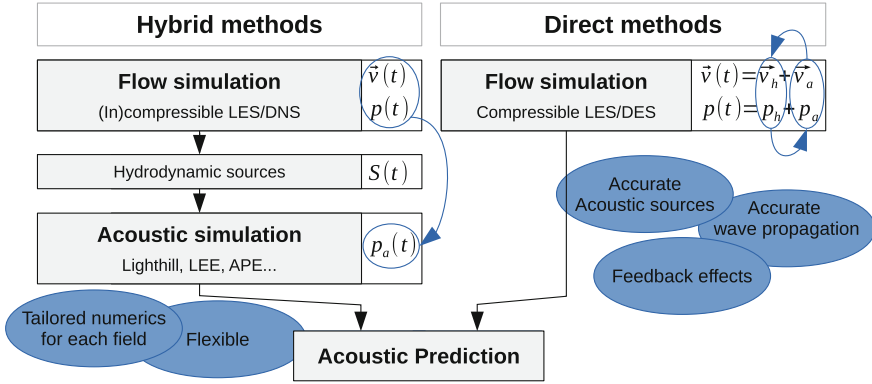
Fig. 2 Direct and hybrid acoustic simulation strategies, with permission from Frank (2016)

The decoupling of the two physical phenomena allows the development of numerical schemes tailored to the specific area of application. The governing equations, solution algorithms and discretizations can be chosen independently for each step to optimize their respective efficiency. For the hydrodynamic simulation, time-resolving simulation methods (DNS, LES, unsteady RANS) are used to compute a space-time evolution of the flow field from both the compressible and incompressible Navier–Stokes equations. From this solution, time- and space-dependent acoustic source terms for the subsequent acoustic simulation are generated. These source terms are then re-introduced in the second simulation step, for which different formulations for the propagation of acoustics exist. Many of these formulations are based on the inhomogeneous wave equation derived by Lighthill (1952) or a perturbation formulation of the Euler equations, and differ in their assumed relationship between the hydrodynamics and the source term and in the assumed state of the base flow. Beyond the flexibility in the choice of the equations and discretizations, the hybrid approach also allows the selection or truncation of the source term region and thus the isolation of different acoustic effects in the (computationally much cheaper) second step.

Besides the additional complexity stemming from the handling of the source term and the two computational schemes, the most serious drawback of the hybrid approach are its inherent underlying assumptions, which for example rule out acoustic feedback loop like the one discussed in Sect. 4.3. Also, if no clear scale separation exists (e.g. in high Mach number flows), the hybrid approach loses its validity and makes the designation of source terms ambiguous. Figure 2 summarizes the conceptual differences between direct and hybrid acoustic simulation strategies.

2   Numerical Schemes for Direct Acoustics

In this section, we will give a brief overview of the requirements and challenges for the scale resolving simulation of acoustics. Schemes used in direct methods, where the hydrodynamic and acoustic scales are resolved (see Figs. 1 and 2), clearly need good

scale-resolving capabilities. To a lesser extent, the requirements on the numerical scheme also apply to hybrid methods, in which hydrodynamic source computations and acoustic simulation are split into two subsequent simulations, which allow an independent discretization of each problem. Still, since the basic requirement is that of a multi-scale problem, essentially the same challenges to the discretization schemes exist.

2.1 Physical Considerations

As discussed in Sect. 1, the aeroacoustic sources stem from the hydrodynamic fluctuations, i.e. the frequency of the small scales of turbulent motion determines the bandwidth of the acoustics. From Kolmogorov's theory (1999), the relationship between the spatial scales in fully developed turbulence is known to be

$$\frac{L}{\eta} \sim Re^{3/4},\tag{1}$$

i.e. the bandwidth between the largest or energy-carrying scales L and the smallest or dissipative scales η is determined by the Reynolds number. To estimate the local time scale associated with each wavenumber, an eddy-turnover-frequency (Colonius and Lele 2004) can be constructed on dimensional grounds from

$$f(k) = \frac{1}{\tau(k)} = \sqrt{k^3 E(k)},\tag{2}$$

where $E(k)$ denotes the one-dimensional spectrum of kinetic energy. Using a von Kármán–Kraichnan model spectrum for $E(k)$, Fig. 3 depicts the eddy-turnover-frequency $f(k)$ for different Reynolds numbers. As a direct consequence of the increase in spatial bandwidth with Re, the range of f and its magnitude also increase, which results in a broader range of acoustic emission and shorter acoustic wavelengths. Thus, since the turbulent scales of motion and the noise generation mechanism are so closely coupled, the numerical simulation of noise generation is faced with the same issues as the scale-resolving simulation of (compressible) turbulence: The range of scales that can be resolved without the additional assumptions or models is limited by the wave propagation properties of the numerical scheme and its computational efficiency. In addition, in particular for low Mach number flows, the inefficient transfer from hydrodynamic to acoustic energy results in large discrepancies between the flow and acoustic energy, which makes the latter even more susceptible to approximation errors. One situation where LES can be applied successfully to acoustic problems without an explicit closure approach is when the dominant source mechanisms are associated with the 'large' flow scales, i.e. when the sound producing features of the flow are within in the range of scales that are well-resolved in an LES and essentially decoupled from the model errors. One example of such a situation will be given in Sect. 4.3.
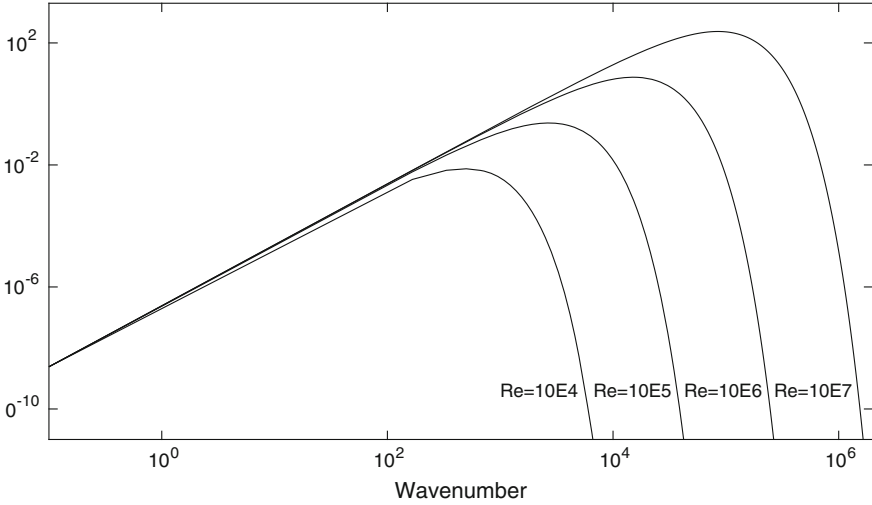
Fig. 3 Eddy turnover frequency for high Reynolds number flows

## 2.2 Discretization Methods for Scale Resolving Simulations

The requirements for LES and DNS discussed above and those for noise computation are of the same nature. They both imply that a numerical scheme of high or spectral order of accuracy is favorable, since these provide favorable wave resolution properties due to low approximation errors. A straightforward extension of Eq. (1) to three dimensions gives the following estimate for the number of degrees of freedom required for the spatial discretization operator of a DNS at a given Reynolds number

$$N_{3D} = \left(\frac{L}{\eta/n_{ppw}} \right)^3 \sim n_{ppw}^3 \, Re^{9/4}. \tag{3}$$

Here, n_{ppw} is the number of solution or grid points required to resolve structures of size η with a given approximation error. It thus can be interpreted as a number of points per wavelength criterion, which directly represents the numerical accuracy per degree of freedom. A more refined analysis leads to a more stringent requirement of $N_{3D} \sim n_{ppw}^3 \, Re^{37/14}$ (Choi and Moin 2012). Considering not only the spatial degrees of freedom, but also the fact that the characteristic time scale of the dissipation scales is directly proportional to η, the total computational cost in terms of spatial and temporal degrees of freedom N_{total} becomes

$$N_{total} \sim n_{ppw}^4 \, Re^3. \tag{4}$$

Clearly, not only the physical complexity of the problem can make or break a simulation through the dependence on Re, but also the numerical capabilities of the
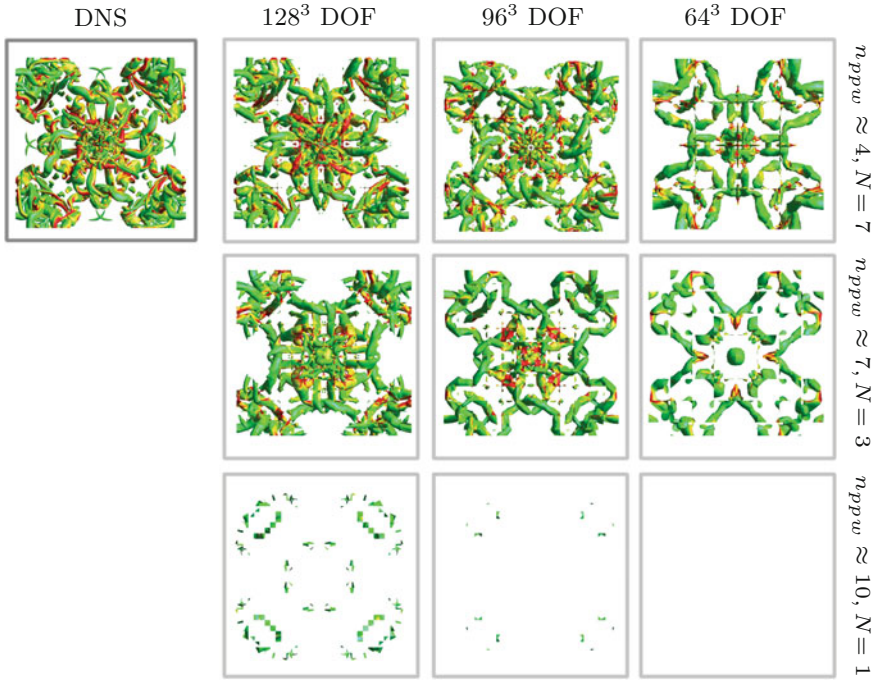
Fig. 4 Visualization of vortical structures of the Taylor–Green vortex at $Re = 1600$ via the λ_2 criterion for different discretizations

discretization scheme can be decisive. Thus, a fundamental demand for efficient numerical simulation of all or a subset of the scales of turbulent motion can be formulated as: The number of degrees of freedom or grid points required to accurately resolve the smallest occurring relevant scale, n_{ppw}, must be minimized. By their design, schemes of a high approximation order achieve this purpose for smooth problems. But also for under-resolved situations, these schemes can retain their low approximation errors over a wide range of resolved scales (Beck et al. 2014).

Figure 4 highlights the influence of the chosen discretization on the scale-resolving capabilities for turbulent flows. Shown is a visualization of the vortical structures of the Taylor–Green vortex at $Re = 1600$ and at non-dimensional time $t = 9$. The vortices are identified by the $\lambda_2 = -0.3$ criterion. Since the problem contains a number of symmetries, only one eighth of the full domain is shown. All computations are conducted with the Discontinuous Galerkin method presented in Sect. 3, where the polynomial degree N of the solution approximation and thus the order of accuracy can be chosen arbitrarily. In the upper left corner, the DNS result, computed with 512^3 DOF, is shown as a reference. In the 3×3 matrix to the right, each column corresponds to a fixed spatial number of DOF, and each row corresponds to a value of n_{ppw}. In other words, each row represents an h-refinement/coarsening of a given discretization, while each column shows different combinations of number of

elements and degree N. For example, in the column corresponding to 128^3 DOF, the first row entry is computed on a grid with 16^3 elements. In each element, the solution is approximated by a tensor product of one-dimensional polynomials of degree $N = 7$, leading to a total of 128^3 DOF. This high order approximation has a low value of $n_{ppw} \approx 4$ (Gassner and Kopriva 2011). In the second row, the number of elements is doubled per dimension to 32^3, while N is reduced to 3 with $n_{ppw} \approx 7$ leading again to 128^3 DOF.

Comparing the columns in Fig. 4, it is evident that as expected the solution quality deteriorates with respect to the DNS when the overall resolution is reduced. Grid artifacts become visible, and the small scale turbulent structures disappear, while the larger scale structures become smeared by the numerical diffusion. The more interesting observation from this plot comes from comparing the rows among each other. The n_{ppw} criterion clearly determines the scale resolving capabilities of the scheme, and for the same number of DOF, the solution produced by the second order scheme is completely dominated by the numerical errors.

From this discussion it follows that high order schemes are advantageous when considering acoustic sources and wave transport. However, high order accuracy and a low n_{ppw} is not the only determining factor for computational efficiency, but an important one. There are various ways in which discretizations achieve high order approximations, but they differ in other important aspects that overall determine their suitability for large scale direct noise computation. In the following, a brief overview of the typical discretization strategies is given.

For finite volume (FV) schemes, the integral form of the conservation equation is solved at a discrete level, i.e. the evolution of the mean in each grid cell is computed. Information exchange between the elements occurs via a numerical flux function. This ensures local conversation and introduces stability for underresolved problems and strong gradients. To achieve a higher order approximation, a reconstruction step is added, which reconstructs higher order approximation polynomials from the integral data across given element stencils. The specific methods then differ in the choice of the reconstruction stencils and in the combination or selection of the polynomials. In particular for three-dimensional simulations, this reconstruction process incurs a high computational effort and a complex parallelization. On non-regular grids, the formally high order accuracy is usually not obtained, which negates one main advantage of FV schemes, namely their general suitability for unstructured meshes. Figure 5 highlights the challenges introduced by the reconstruction process.

High order finite difference (FD) schemes are based on analytical differentiation of an interpolating polynomial. Thus, they inherit the simplicity of the interpolation operation, but also its drawbacks. For advection dominated problems, stencil upwinding or filtering is needed for stabilization. Achieving a high approximation order is straight-forward by stencil extension, but makes parallelization particularly demanding (alternatively, compact FD schemes solve a local linear system of equations). One subfamily of FD schemes are the dispersion relation preserving schemes, which sacrifice the theoretical order of convergence for improved phase and amplitude errors (Tam and Webb 1993; Bogey and Bailly 2004). The main drawback of FD
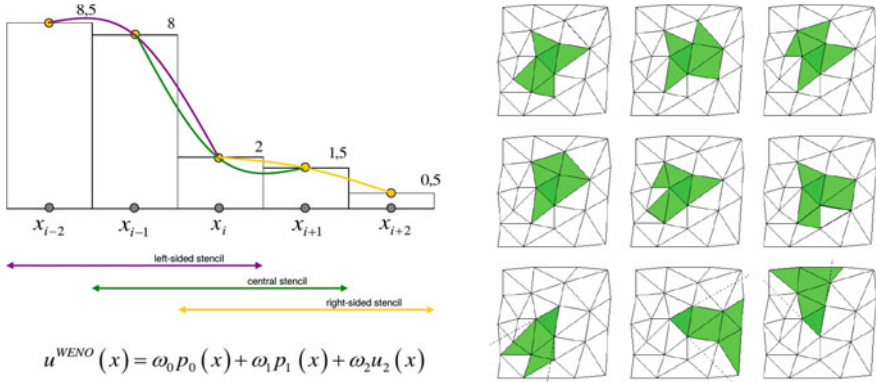
Fig. 5 *Left*: 1D stencil for quadratic reconstruction, *Right*: stencil choices for quadratic reconstruction in 2D

schemes is their reliance on structured grids and the complex integration of boundary conditions.

Global spectral (GS) methods form another class of schemes that have by design very favorable n_{ppw} values, down to the theoretical limit of 2 for Fourier-basis based methods. They have in common that the solution in the domain is approximated by a unique global solution representation, i.e. their stencil includes all available information. The residual is either minimized in an L_2-projection sense or at discrete solution points, leading to the Spectral-Galerkin-type schemes and the Spectral-Collocation-type schemes. These methods have been widely used in basic turbulence research, mainly for the incompressible Navier–Stokes equations (Yokokawa et al. 2002). For compressible problems, additional stabilization mechanism are required, e.g. Hussaini et al. (1985), Shebalin (1993). The global nature of the approximation makes parallelization non-trivial and costly compared to other methods. The main drawback of these methods is however their restriction to a single domain geometry.

In contrast to these global spectral methods, the class of high order finite element (FE) spectral methods decomposes the computational domain into grid cells or elements, which can be arranged in an unstructured, non-conforming way, akin to FV grids. Based on the chosen ansatz, this class can be split into continuous (for a globally continuous ansatz) and discontinuous (for an element-local ansatz) Galerkin methods. Both groups allow an easy way to increase the approximation order and thus reduce n_{ppw}. Continuous Galerkin methods are employed for incompressible flows mainly, and require additional stabilization for hyperbolic problems. Discontinuous Galerkin methods gain stability for compressible problems through the numerical flux function that penalizes inter-element discontinuities. In addition, the coupling through the fluxes and not the solution itself reduces the communication footprint of the method, and makes its parallelization straightforward. These methods thus combine high order accuracy, geometric flexibility and computational efficiency.

Table 1 Comparison of features of discretization schemes for direct acoustic computation

	n_{ppw}	Costs/DOF	Geometry	Parallelization	Stability
GS	✓	∼	−	∼	−
CG/DG	✓	✓	✓	✓	(✓)
FD	✓	✓	∼	✓	✓
FV HO	✓	∼	✓	∼	✓

Table 1 summarizes the advantages and disadvantages discussed here. For direct noise computation in complex domains, a single domain method is not practical so discretizations that rely on a global solution representation are ruled out. Furthermore, if geometric flexibility is required, only discretization strategies that naturally support unstructured meshing are viable options. Among these, DG methods combine high order accuracy without increasing stencil size and inherent suitability for hyperbolic problems, which make it a very suitable candidate as a base scheme for investigating noise generation. In the following section, we will present the numerical and implementation details of such a DG framework.

3 Discontinuous Galerkin Spectral Element Method

In this section, we present the details of a special variant of the DG method, namely the Discontinuous Galerkin Spectral Element Collocation Method (DGSEM). Discontinuous Galerkin methods in general can be interpreted as a hybrid of high order FE methods and FV methods, which gives them a number of favorable properties for scale-resolving simulations:

- Spectral accuracy for smooth problems when increasing the degree of the local ansatz (p-refinement), which results in low n_{ppw} requirements, as discussed in Sect. 2.2
- Natural support of arbitrarily shaped grid elements, which can be connected in an unstructured, non-conforming way
- Local grid refinement or basis enrichment in regions of interest (h/p-refinement)
- Stability for hyperbolic problems with discontinuities through numerical flux functions
- Local conservation for each element
- Weak imposition of the boundary conditions through fluxes
- Efficient parallelization due to minimal inter-element coupling
- Orthogonal hierarchical bases which resolve a large wave range within an element and which can be exploited in multiscale modeling

DG methods have a relatively recent research history. They were introduced by Reed and Hill (1973) in 1973 for linear advection problems of neutron transport on triangular meshes and analyzed by Lesaint and Raviart (1974). Research then lay dormant for about two decades, until Cockburn and Shu provided a systematic extension to systems of non-linear conversation equations (Cockburn and Shu 1991, 1989; Cockburn et al. 1989, 1990) such as e.g. the compressible gas dynamics. Bassi and Rebay were the first to introduce a mixed finite element type approach for the discontinuous Galerkin discretization of viscous flow problems and extended the DG method to the compressible Navier–Stokes equations (Bassi and Rebay 1997). Collis in 2002 was the first to use a high order DG method ($p = 6$) for the DNS of a weakly compressible turbulent channel flows at a low Reynolds number, with about 13 mio DOF for his finest mesh (Collis 2002).

Since DG methods are closely related to high order FE methods, the core of the method can be summarized in two steps: The projection operator of the variational formulation and the inversion of the mass matrix. The discretization and implementation choices for these two steps, together with the choice of the element topography, lead to different DG formulations. Among these (spatial) choices are the basis functions (e.g. Lagrange or Legendre-type polynomials), the approximation space spanned by these functions in multi-dimensions (a tensor-product approach or a full order basis), the choice of the quadrature method, the weak or strong DG-formulation, the discretization choices for the inviscid and viscous surface fluxes and the treatment of non-linearities. The temporal integration introduces another level of possible choices.

Among these different variants, the Discontinuous Galerkin Spectral Element Collocation Method (DGSEM) (Kopriva 2009; Hindenlang et al. 2012) combined with an explicit time integration scheme has shown to be highly effective and competitive for scale-resolving simulations.

3.1 Basic DG Discretization

In this section, we derive details and specific implementation choices of the Discontinuous Galerkin Spectral Element Collocation Method for a system of hyperbolic-parabolic conservation equations, following Kopriva (2009) and Hindenlang et al. (2012). Since the main focus is the direct noise computation, we use the compressible Navier–Stokes equations in physical space $\mathbb{R}^3$ as an example.

Compressible Navier–Stokes Equations The temporal and spatial evolution of a viscous, compressible fluid is governed by the conservation statements for mass, momentum and energy. In conservative form this set of partial differential equations for a Newtonian fluid is given as

$$\frac{\partial \rho}{\partial t} + \frac{\partial \left(\rho u_j\right)}{\partial x_j} = 0,$$

$$\frac{\partial \left(\rho u_i\right)}{\partial t} + \frac{\partial \left(\rho u_i u_j + p\delta_{ij}\right)}{\partial x_j} = \frac{\partial \sigma_{ij}}{\partial x_j},$$

$$\frac{\partial \left(\rho e\right)}{\partial t} + \frac{\partial \left[\left(\rho e + p\right) u_j\right]}{\partial x_j} = -\frac{\partial q_j}{\partial x_j} + \frac{\partial \left(\sigma_{ij} u_i\right)}{\partial x_j}. \tag{5}$$

Here, the Einstein summation convention applies, δ_{ij} denotes the Kronecker delta function and $i, j = 1, 2, 3$. The conservative variables of mass, momentum and energy are $U = [\rho, \rho u_1, \rho u_2, \rho u_3, \rho e]$, where ρ denotes the density, u_i the ith component of the velocity vector and the total energy ρe is given by

$$\rho e = \rho \left(\frac{1}{2} u_i u_i + c_v T\right). \tag{6}$$

Herein, c_v and T denote the specific heat at constant volume and the temperature, respectively. The equation of a perfect gas is used to close the system:

$$p = \rho R T, \quad \gamma = \frac{c_p}{c_v}, \tag{7}$$

with $R = c_p - c_v$ as the specific gas constant, the pressure p and the adiabatic exponent γ. The viscous stress tensor σ_{ij} is a function of the viscosity μ (which itself is dependent on temperature) and the velocity gradient tensor

$$S_{ij} = \frac{\partial u_i}{\partial x_j} + \frac{\partial u_j}{\partial x_i} - \lambda \delta_{ij} \frac{\partial u_k}{\partial x_k}. \tag{8}$$

The bulk viscosity coefficient λ is commonly chosen to be $\frac{2}{3}$, which removes the trace from S_{ij}. The remaining unknown in Eq. (5) is the definition of the heat flux vector q_j as

$$q_j = -k \frac{\partial T}{\partial x_j}, \quad \text{with } k = \frac{c_p \mu}{Pr}, \tag{9}$$

where Pr denotes the Prandtl number of the fluid.

In vectorial form, Eq. (5) can be recast as

$$\begin{aligned}
&\frac{\partial U}{\partial t} + \frac{\partial}{\partial x} F^c(U) + \frac{\partial}{\partial y} G^c(U) + \frac{\partial}{\partial z} H^c(U) \\
&- \frac{\partial}{\partial x} F^v(U, \nabla_x U) - \frac{\partial}{\partial y} G^v(U, \nabla_x U) - \frac{\partial}{\partial z} H^v(U, \nabla_x U) = 0
\end{aligned} \tag{10}$$

with the vector of conserved variables U and the associated inviscid and viscous physical fluxes $\{F^c, G^c, H^c\}$ and $\{F^v, G^v, H^v\}$. Collecting the directional fluxes, this can further be simplified to the standard compact form of a conservation law

$$
\begin{aligned}
\frac{\partial U}{\partial t} + \nabla_x \cdot \vec{F}^c(U) - \nabla_x \cdot \vec{F}^v(U, \nabla_x U) &= 0, \\
\frac{\partial U}{\partial t} + \nabla_x \cdot \vec{F}(U, \nabla_x U) &= 0.
\end{aligned}
\tag{11}
$$

Together with suitable initial and boundary conditions, Eq. (11) describes a system of conservation equation of hyperbolic-parabolic type, that can be now be discretized by the DGSEM method.

Spatial Discretization In order to solve this system of equations, a discretization of the computational domain consisting of non-overlapping elements is defined. In the DGSEM method, the type of elements is restricted to hexahedral cells which support a tensor product basis. The elements can be connected in a fully unstructured way. This restriction of the element type can be ameliorated by the use of non-conforming grids, but in general it makes the grid generation process more costly.

Once the grid has been created, each element in the physical domain is then mapped to a unit reference element $E \in [-1, 1]^3$ with coordinates $(\xi^1, \xi^2, \xi^3)^T$. The associated mapping function $\vec{x}(\vec{\xi})$ from reference to physical space is approximated as a polynomial itself and is then used to calculate the Jacobian $J(\vec{\xi}) = \det(\frac{\partial \vec{x}}{\partial \vec{\xi}})$. Clearly, for the mapping to be defined and invertible, $J(\vec{\xi})$ has to be positive everywhere, which can be challenging for non-linear mappings of curved elements (Hindenlang 2014). The main reason for the mapping step is to be able to define the operator itself in reference space, which means that a single shared set of basis functions and quadrature coefficients for each element exists.

The resulting individual element-based mapping is then used to transform Eq. (11) to reference space

$$
U_t + \frac{1}{J(\vec{\xi})} \nabla_\xi \cdot \vec{\mathcal{F}}(U, \nabla_x U) = U_t + \frac{1}{J(\vec{\xi})} \nabla_\xi \cdot (\vec{\mathcal{G}}(U) - \vec{\mathcal{H}}(U, \nabla_x U)) = 0, \quad (12)
$$

where $J(\vec{\xi}) := \vec{a}_1 \cdot (\vec{a}_2 \times \vec{a}_3)$ is again the Jacobian of the mapping $\vec{x}(\vec{\xi})$, calculated from the covariant basis vectors $\vec{a}_l := \frac{\partial \vec{x}}{\partial \xi^l}$. The covariant transformed fluxes are given by

$$
\mathcal{F}^l := J\vec{a}^l \cdot \vec{F}, \quad l = 1, 2, 3,
\tag{13}
$$

with the metric terms

$$
J\vec{a}^l := \vec{a}_k \times \vec{a}_m \quad (l, k, m) \text{ cyclic.}
\tag{14}
$$

The way the metric terms are discretized and implemented is important for the free-stream preserving property of the resulting method. We refer to Kopriva (2006) for

a discussion. This property ensures that the divergence operator remains zero for a spatially constant flux on a discrete level. Besides conservation, this property is of particular importance for acoustic propagation, where the energy of the acoustic waves is considerably smaller than that of the hydrodynamics and can easily be overwhelmed by small scale error terms.

Since the equation for each element is now defined in a common reference element, a shared polynomial basis can now be chosen. In DGSEM, the solution vector within each element is approximated by a tensor product of 1-D Lagrange polynomials ℓ^N of degree N

$$U(\vec{\xi}, t) \approx \sum_{i,j,k=0}^{N} \hat{U}_{ijk}(t) \psi_{ijk}^{N}(\vec{\xi}), \qquad \psi_{ijk}^{N}(\vec{\xi}) = \ell_i^N(\xi^1) \ell_j^N(\xi^2) \ell_k^N(\xi^3), \qquad (15)$$

where $\hat{U}_{ijk}(t)$ are time dependent nodal degrees of freedom and $\ell_i^N(\xi)$ denotes the standard Lagrange polynomial of degree N defined by a nodal set $\{\xi_i\}_{i=0}^{N} \subset [-1; 1]$:

$$\ell_i^N(\xi) = \prod_{j=0; j \neq i}^{N} \frac{\xi - \xi_j}{\xi_i - \xi_j}. \qquad (16)$$

A nodal basis offers the advantage of direct knowledge of the interpolant at its nodes, while its counterpart, a modal basis, would require the evaluation of the full basis. In principle, any set of pairwise unique nodes could be chosen to define the interpolation basis in Eq. (16), as long as the resulting interpolation is stable and has a favorable Lebesque constant. The core idea of the DGSEM method is to collocate the interpolation nodes with those that support a quadrature rule of sufficient accuracy. By this choice, the quadrature itself does not require any evaluation of the basis, and - when extending the basis in a tensor-product - becomes a sum of one-dimensional operations in multiple dimensions. Details on this will be demonstrated in Sect. 3.2.

Since the occurring mass matrix is of degree $\sim \xi^{2N}$, the $N + 1$ Gauss–Legendre quadrature points $\{\xi_i\}_{i=0}^{N}$ are chosen as interpolation nodes, as the associated quadrature is exact for this integrand. Another possible choice would be Gauss–Lobatto–Legendre points, leading to a slightly less efficient and accurate scheme due to inexact integration of the mass matrix (Kopriva and Gassner 2010). Now that the approximation of the solution vector U is in place, the discrete transformed flux $\vec{\mathcal{F}}$ can be chosen in a similar manner

$$\mathcal{F}^l(\vec{\xi}) \approx \sum_{i,j,k=0}^{M} \hat{\mathcal{F}}_{ijk}^l \psi_{ijk}^M(\vec{\xi}), \quad l = 1, 2, 3 \qquad (17)$$

$$\hat{\mathcal{F}}_{ijk}^l = \mathcal{G}^l(U) - \mathcal{H}^l(U, \vec{\nabla}_x U) \mid_{\vec{\xi}_{ijk}} \qquad (18)$$

with $\psi_{ijk}^M(\vec{\xi}) = \ell_i^M(\xi^1) \ell_j^M(\xi^2) \ell_k^M(\xi^3)$. Note that the fluxes are again represented by an interpolation polynomial, but defined on $M + 1$ Gauss–Legendre quadrature points,

with $M \geq N$. This implementation allows for a consistent integration of the non-linear fluxes (Kirby and Karniadakis 2003). The choice of M depends on the non-linearity of the flux for under-resolved calculations. For the classical DGSEM, $M = N$ is chosen, which leads to a collocation of solution and fluxes on the same nodes and thus a very efficient implementation.

Now that the domain discretization and the solution and flux approximations have been defined, we can derive the variational formulation of the problem and from it; first the DG formulation, and then the DG discretization scheme. We start by multiplying Eq. (12) by a test function $\phi(\vec{\xi})$ which is taken from the same space as the basis functions. Integrating over the reference element E to leads to the variational formulation in reference space

$$\int_E \left(JU_t + \nabla_\xi \cdot \vec{\mathcal{F}}(U, \nabla_x U) \right) \phi(\vec{\xi}) \, d\vec{\xi} = 0. \tag{19}$$

This formulation can be interpreted as an L_2 projection of the residual onto the space of test functions, which enforces orthogonality. Note that so far, no connection to the neighboring elements exist. To remedy this, the second term is rewritten using spatial integration by parts, i.e. the flux divergence is reworked using the product rule of differentiation. Applying the Gauss theorem, the so-called weak formulation of the DG discretization is obtained:

$$\int_E JU_t \phi \, d\vec{\xi} + \oint_{\partial E} \underbrace{\left(\mathcal{G}_n^* - \mathcal{H}_n^* \right)}_{\mathcal{F}_n^*} \phi \, ds - \int_E \vec{\mathcal{F}}(U, \nabla_x U) \cdot \nabla_\xi \phi \, d\vec{\xi} = 0, \tag{20}$$

where $\mathcal{G}_n^*$ denotes the surface normal numerical flux function for the inviscid terms, given by $\mathcal{G}_n^* := \mathcal{G}_n^*(U^+, U^-)$ and superscripts $\pm$ denote the values at the grid cell interface from the neighbor and the local grid cell, respectively. Note that in the volume integral, the flux is no longer required to be differentiable and can be evaluated from information within each grid element, while the new surface integral now contains a numerical flux function to find a unique interface flux from two generally discontinuous left and right states. For the inviscid numerical flux, several well-known flux functions derived for FV formulations are possible, which ensure consistency and uniqueness of the numerical flux. Within the DG community, the most commonly applied flux functions are Godunov's method, the local Lax–Friedrichs or Rusanov flux and Roe's approximate Riemann solver (Toro 1999). The choice of $\mathcal{H}_n^*$ will be discussed in Sect. 3.3.

3.2 The DGSEM Operator

So far, in the derivation of the variational form Eq. (19) and the weak DG formulation Eq. (20), the specific choices made for DGSEM did not come into play. In the

following section, a brief discussion of the DGSEM operator will be given, which is intended to highlight the most important aspects in terms of efficiency. A full, very detailed derivation of the DGSEM operator is given by Hindenlang et al. (2012). As defined in Eqs. (15) and (17), the solution and the flux are represented by tensor products of one-dimensional Lagrange interpolating polynomials, associated with either one-dimensional Legendre–Gauss or Legendre–Gauss–Lobatto quadrature points. The Lagrange property of the basis functions on these nodes makes the evaluation of the basis at these points trivial, as the solution is represented by a nodal interpolation. The evaluation of the inner products is then achieved by the corresponding quadrature rule, which reverts to a sequence of three one-dimensional sums along a reference coordinate line instead of a volume operation including all the element-local solution points. This can be understood as a transfer of the tensor product structure of the basis directly to the operator itself by choosing quadrature and interpolation nodes as described above. This choice reduces the number of operations from $\mathcal{O}(N+1)^6$ for a standard DG formulation to $\mathcal{O}(N+1)^4$ for DGSEM.

We demonstrate this concept of operation reduction by applying the DGSEM formulation to the first volume integral, containing the time derivative of the degrees of freedom, from Eq. (20). First, we insert the ansatz for the solution (Eq. (15)) into the semi-discrete form and choose the test function ϕ from the space of Lagrange polynomials of degree N as ψ_{ijk}^N with associated $N+1$ Legendre–Gauss nodes $\{\xi_i\}_{i=0}^N$

$$\int_E J(\vec{\xi})U_t\phi\,d\vec{\xi} = \int_E J(\vec{\xi})\left(\frac{\partial}{\partial t}\sum_{r,s,t=0}^N \hat{U}_{rst}(t)\psi_{rst}^N(\vec{\xi})\right)\psi_{ijk}^N\,d\vec{\xi}. \tag{21}$$

The integral over the reference space is now split into the coordinate directions and then replaced by Legendre–Gauss quadrature with associated weights ω:

$$\int_E J(\vec{\xi})U_t\phi\,d\vec{\xi} = \int_{-1}^1\int_{-1}^1\int_{-1}^1 J(\vec{\xi})\left(\frac{\partial}{\partial t}\sum_{r,s,t=0}^N \hat{U}_{rst}(t)\psi_{rst}^N(\vec{\xi})\right)\psi_{ijk}^N(\vec{\xi})d\vec{\xi}^1 d\vec{\xi}^2 d\vec{\xi}^3$$

$$= \sum_{\alpha,\beta,\gamma=0}^N J(\vec{\xi}_{\alpha\beta\gamma})\left(\frac{\partial}{\partial t}\sum_{r,s,t=0}^N \hat{U}_{rst}(t)\underbrace{\ell_r^N(\xi_\alpha^1)}_{=\delta_{r\alpha}}\underbrace{\ell_s^N(\xi_\beta^2)}_{=\delta_{s\beta}}\underbrace{\ell_t^N(\xi_\gamma^3)}_{=\delta_{t\gamma}}\right)\psi_{ijk}^N(\vec{\xi}_{\alpha\beta\gamma})\omega_\alpha\omega_\beta\omega_\gamma$$

$$= \sum_{\alpha,\beta,\gamma=0}^N J(\vec{\xi}_{\alpha\beta\gamma})\frac{\partial}{\partial t}\hat{U}_{\alpha\beta\gamma}(t)\underbrace{\ell_i^N(\xi_\alpha^1)}_{=\delta_{i\alpha}}\underbrace{\ell_j^N(\xi_\beta^2)}_{=\delta_{j\beta}}\underbrace{\ell_k^N(\xi_\gamma^3)}_{=\delta_{k\gamma}}\omega_\alpha\omega_\beta\omega_\gamma$$

$$= \underbrace{J(\vec{\xi}_{ijk})\omega_i\omega_j\omega_k}_{pre-compute}\frac{\partial}{\partial t}\hat{U}_{ijk} \quad \forall\,i,j,k=0,\ldots,N. \tag{22}$$

In Eq. (22), the Kronecker delta functions result from the Lagrange property and thus reduce the associated summation to a single evaluation. Note that the mass matrix is diagonal also for Legendre–Gauss–Lobatto nodes, making the chosen basis both *nodal* as well as *discretely orthogonal*. The Jacobian of the geometry mapping is treated in a collocation way in this approach, i.e. it is not integrated exactly if the mapping is beyond bi-linear. In this case, an additional error akin to mass-lumping for Gauss–Lobatto integration of the mass matrix is introduced.

From an efficiency point of view, Eq. (22) demonstrates how the three-dimensional integrals reduce to point-wise evaluations in DGSEM. For each of the $(N + 1)^3$ degrees of freedom $\hat{U}_{ijk}$ per element, just a single multiplication with a pre-computed term is necessary, due to the "folding" of the three-dimensional integral based on the tensor-product structure instead of the evaluation of a three-dimensional integral and inversion of a full mass matrix.

For the surface and flux volume integrals in Eq. (20), a similar reduction in operations can be shown, where the volume integral retains an operation count of $(N + 1)$ multiplications per DOF, as the the derivatives of the basis functions do not support the Lagrange property. Further details and a full discretization of the operator can be found in Hindenlang et al. (2012). The semi-discrete form of the DGSEM operator in three dimensions is given as

$$-J_{ijk}\left(\hat{U}_{ijk}\right)_t = \left(\sum_{\alpha=0}^{N}\hat{D}_{i\alpha}\hat{\mathcal{F}}^1_{\alpha jk}\right) + \left([\mathcal{F}^*\hat{s}]^{+\xi^1}_{jk}\hat{\ell}_i(+1) + [\mathcal{F}^*\hat{s}]^{-\xi^1}_{jk}\hat{\ell}_i(-1)\right) +$$
$$\left(\sum_{\beta=0}^{N}\hat{D}_{j\beta}\hat{\mathcal{F}}^2_{i\beta k}\right) + \left([\mathcal{F}^*\hat{s}]^{+\xi^2}_{ik}\hat{\ell}_j(+1) + [\mathcal{F}^*\hat{s}]^{-\xi^2}_{ik}\hat{\ell}_j(-1)\right) + \quad (23)$$
$$\left(\sum_{\gamma=0}^{N}\hat{D}_{k\gamma}\hat{\mathcal{F}}^3_{ij\gamma}\right) + \left([\mathcal{F}^*\hat{s}]^{+\xi^3}_{ij}\hat{\ell}_k(+1) + [\mathcal{F}^*\hat{s}]^{-\xi^3}_{ij}\hat{\ell}_k(-1)\right) ,$$

with the precomputable one-dimensional operators defined as

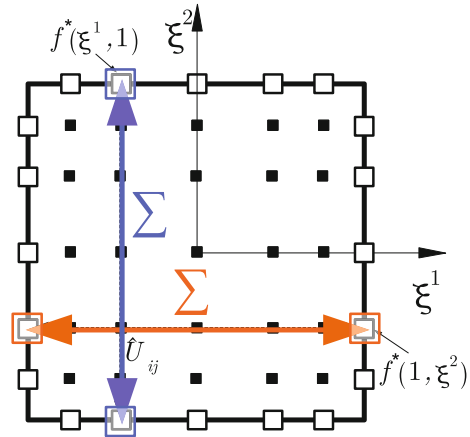$$D_{ij} = \frac{d\ell_j(\xi)}{d\xi}\bigg|_{\xi=\xi_i},$$
$$\hat{D}_{ij} = -D_{ji}\frac{\omega_j}{\omega_i}, \quad i, j = 0, \ldots, N. \quad (24)$$

The weighted basis functions are given accordingly by

$$\hat{\ell}_i = \frac{\ell_i}{\omega_i}, \quad i = 0, \ldots, N, \quad (25)$$

and $\hat{s}$ is the surface element, relating the physical to the reference surface.

Equation (23) highlights how the tensor-product basis and collocation of quadrature and interpolation translates to a tensor-product operator and thus becomes computationally highly efficient. The three-dimensional operator essentially collapses to a sequence of three consecutive one-dimensional operators.

Figure 6 visualizes the operator and the involved nodes for two dimensions. The computation of the residual at a given node $\hat{U}_{ij}$ involves essentially three steps: The contribution to the surface integral requires the prolongation of the solution to the element-faces and the subsequent evaluation of the numerical fluxes as a function of the state in the neighboring element. This results in four flux evaluations in 2D. Secondly, the volume contribution is computed by numerical quadrature along two coordinate lines. The third step, the inversion of the mass matrix, is trivially given due to the orthogonality of the basis.

3.3 Approximation of Viscous Fluxes

Returning to Eq. (20), the last missing term to be defined is the numerical approximation for the viscous flux term $\mathcal{H}_n^*$. This term introduces a dependence on the gradient of the solution. The treatment of the gradient terms in the context of DG approximations was first tackled by Bassi and Rebay (1997), who introduced a mixed finite element approximation, in which the gradients are approximated in the same discontinuous polynomial space as the solution. They also showed that a local evaluation of the gradient leads to instabilities, and that some form of "lifted" gradient, containing information from both adjacent elements, is needed.

To derive the mixed formulation, the system of governing equations is rewritten as a corresponding system of first order equations with an auxiliary variable $\vec{S}$ as an approximation of the lifted gradients

$$\vec{S} - \nabla_x U = 0,$$
$$U_t + \nabla_x \cdot \vec{F}(U, \vec{S}) = 0. \tag{26}$$

Applying the discretization steps outlined above to derive a weak DG discretization of the auxiliary equation leads to

$$c = 1, \ldots, 5 : \quad \int_E J \vec{s}_c \phi \, d\vec{\xi} + \oint_{\partial E} \vec{\mathfrak{u}}_{c,n}^* \phi \, ds - \int_E u_c \cdot \nabla_\xi \phi \, d\vec{\xi} = 0,$$
$$\int_E J U_t \phi \, d\vec{\xi} + \oint_{\partial E} \left(\mathcal{G}_n^* - \mathcal{H}_n^* \right) \phi \, ds - \int_E \vec{\mathcal{F}}(U, \vec{S}) \cdot \nabla_\xi \phi \, d\vec{\xi} = 0, \tag{27}$$

with the component u_c of the state vector U and its lifting operator $\vec{s}_c$. The numerical flux of the auxiliary equation is $\vec{\mathfrak{u}}_{c,n}^*$, and $\mathcal{H}_n^* = \mathcal{H}_n^*(U^+, U^-, \vec{S}^+, \vec{S}^-)$ denotes the numerical flux function for the viscous terms. Following Bassi and Rebay (1997), we choose

$$c = 1, \ldots, 5 : \quad \mathfrak{u}_{c,n}^* = \left(\alpha_{visc} u_c^+ + (1 - \alpha_{visc}) u_c^- \right) \vec{n}, \tag{28}$$

$$\mathcal{H}_n^* = \left(\alpha_{visc} \mathcal{H}_n(U^+, \vec{S}^+) + (1 - \alpha_{visc}) \mathcal{H}_n(U^-, \vec{S}^-) \right), \tag{29}$$

with $\vec{n}$ denoting the outward pointing surface normal. For a parameter of $\alpha_{visc} = \frac{1}{2}$, this treatment of the viscous fluxes is usually labeled BR1 (first method of Bassi and Rebay 1997).

3.4 Boundary Conditions

Since in DG methods, the coupling between the elements is achieved weakly or indirectly through the numerical flux as a function of the adjacent states, it is natural to extend this approach to the boundary conditions as well. The rationale for this approach is to ensure consistency in the approximation of the internal faces fluxes and the boundary conditions, i.e. to use the same discretization operators for both and thus avoid stability issues (Bazilevs and Hughes 2007). This approach is also applicable to Dirichlet type boundaries, where instead of prescribing a state U directly at the boundary, an appropriate right hand side state U^+ (akin to a ghost cell state) is prescribed. Together with its adjacent neighbor state from within the domain, it is then used to compute the resulting advection boundary flux through the appropriate Riemann solver. The gradients for the diffusive fluxes are chosen according to the specific type of boundary condition.

Collis (2002) investigated the effect of weakly versus strongly imposed Dirichlet conditions for the case of an under-resolved one-dimensional stationary boundary layer problem and turbulent channel flows. He found that the L_2 error norm is greatly
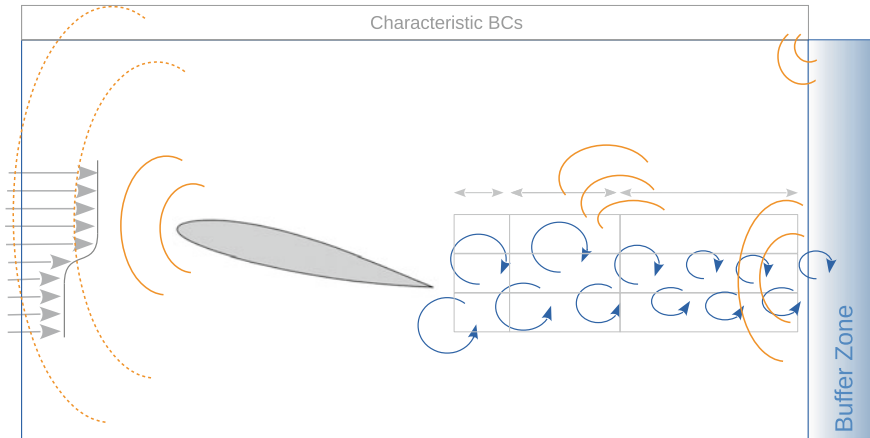
**Fig. 7** Boundary conditions and acoustic disturbance sources

reduced when the boundary conditions are enforced in this weak manner and oscillations near the boundary are avoided. We follow this approach, and we enforce the boundary conditions for Eq. (27) weakly through the prescription of the right hand side state U^+ of the boundary fluxes $\vec{u}_{c,n}^*$, $\mathcal{G}_n^*$ and $\mathcal{H}_n^*$.

Challenges in Aeroacoustics Due to the scale separation between hydrodynamics and acoustics, stable and accurate boundary conditions pose a considerable challenge. In particular, outflow and far field conditions are difficult to handle in subsonic flows, since they are usually artificial boundaries and thus the correct outer state is not known. Especially at the outflow boundary, where large scale non-linear hydrodynamic structures need to exit the domain, a slight error in the boundary condition will act as any gradient in the Lighthill tensor and produce noise radiating from the boundaries into the domain. Figure 7 highlights some of the challenges of applying boundary conditions and sources that may pollute the acoustic field.

Another issue that is not directly related to the boundary condition treatment is the generation of sound waves at gradients of the local resolution, e.g. at stretched or skewed grid cells where waves become more poorly resolved and their non-resolvable energy is radiated again as acoustics. This becomes particularly troublesome for high order discretization with low numerical dissipation.

Across the inflow boundary, the incoming flow state and possible noise disturbances are described. Upstream propagating waves must be able to leave the domain without reflections. Recognizing that these waves are typically of low amplitude, boundary condition types based on linearization and characteristic decomposition work well. This also holds for the parts of the boundary that are approximately parallel to the flow, as long as no large amplitude noise occurs. At the outflow boundary, approaches based on linearization are generally not successful when high amplitude disturbances like turbulent structures encounter the boundary. Without special treatment, the outflow boundary can act as a dominating artificial source and pollute the

Fig. 8 Reflection coefficient
of different boundary
conditions
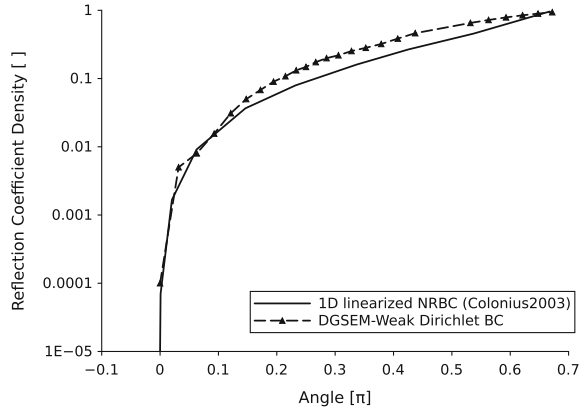
whole acoustic field. No general theoretical method exists to construct non-reflecting boundary conditions in this situation. Instead, an artificial absorbing layer is the most commonly used approach. This layer is placed upstream of the boundary itself and modifies the incoming flow and acoustic field while it is passing through it. The amplitudes of the disturbances are damped towards a "quiet" base flow, which then exits through a linearized boundary condition. While this approach can be very effective and computationally efficient, it introduces a number of user-selectable parameters such as layer width or ramping function and itself can also become reflective. In addition, careful blending of the buffer region with other adjacent boundaries must be implemented to avoid generation of disturbances through a mismatch. Colonius (2004) gives a good overview of possible implementations for ad-hoc solutions, such as sponge zones, perfectly matched layers, fringe and grid stretching.

Boundary Conditions for DG In the following section, we will briefly discuss how the typical boundary conditions discussed above can be treated in the DG context.

Far Field Boundaries As discussed above, the boundary conditions in DG are prescribed weakly through a numerical flux. The choice of this flux function can be adapted to the problem at hand; for the acoustic far field, those that are based on a wave decomposition are a natural choice. The state outside of the domain is fixed to the free-stream state at infinity, and the resulting boundary flux is computed with the adjacent inner state. It has been shown in Flad et al. (2014) that employing Roe's Riemann solver flux function mimics classical one-dimensional linearized characteristic non-reflecting boundary conditions and effectively prevents reflections of acoustic disturbances.

Figure 8 shows the reflection behavior of a planar acoustic wave transported with background velocity $u_0 = 0.5$ and speed of sound $c = 1$, crossing the boundary under different incident angles. It is compared to a 1D linearized local boundary condition proposed by Colonius (2004). The reflection coefficient $max(|\rho_{refl}|)/max(|\rho|)$ vanishes for small angles and drops below 5% for angles smaller than $\approx 25°$.

Outflow Boundaries A simple and robust variant of the absorbing layer discussed above is the sponge zone concept, in which a retarding volume source term is included in the spatial operator

$$U_t = R(U) - d\sigma(\vec{x})(U - U_B), \tag{30}$$

where $R(U)$ represents the discretized Navier–Stokes operator, d controls the magnitude of the source term and $\sigma(\vec{x})$ denotes a ramping function. This ramping function is intended to prevent reflections at the domain - sponge interface and smoothly increases the source term strength towards the domain edges. U_B identifies an acoustically quiet base flow towards which the solution is forced; clearly, if $U_B = U$, the source term vanishes. Suitable choices for U_B are a constant free-stream state or a time-averaged solution from a prior simulation. A flexible and general method to determine a suitable base flow is to generate it from a moving time-average of the solution. This time-average is computed by an exponential temporal filter, which can be written in a simple differential form as

$$\bar{U}_t(t, \Delta) = \frac{U(t) - \bar{U}(t, \Delta)}{\Delta}, \tag{31}$$

This expression only requires storing of one previous base flow states. It is integrated in time alongside the spatial DG operator and thus yields the base flow $U_B = \bar{U}(t, \Delta)$ in every time step. This filter idea has been adopted from the temporally filtered LES by Pruett et al. (2003). The filter width Δ should be set to cover the largest time scales of the flow.

Following Flad et al. (2014) to demonstrate the effectiveness of this sponge method, a 2D isentropic Euler vortex with an initial maximum density perturbation of 13.3% is transported at $Ma = 0.5$ along the x-direction. It is computed without any damping zone and with the adapting sponge approach discussed above. The sponge layer uses a ramping function of width Δx_{SP} which starts at x_0 and uses a polynomial blending given by

$$\sigma(x^*) = 6x^{*5} - 15x^{*4} + 10x^{*3}, \tag{32}$$

and with

$$x^* = \frac{x - x_0}{\Delta x_{SP}} \tag{33}$$

being the local sponge coordinate. The parameters for the sponge zone are $x_0 = 10$, $\Delta x_{SP} = 10$, $d = 0.1$, $\sigma(x^*)$ equals 0.1 for $20 \leq x \leq 25$ and $\Delta = 20$. Figure 9 gives a qualitative impression of the reflection entering the computational domain of interest $x < 10$ without and with a sponge zone, showing a significant reduction of reflected acoustics for the latter case.

As shown by Akervik et al. (2006), using a moving temporal average as a base state has the additional advantage of not altering the steady state solution. This implies that the sponge zone can be initiated very closely to the region of interest, which reduces computational costs compared to other zonal concepts. In addition, this reduces the
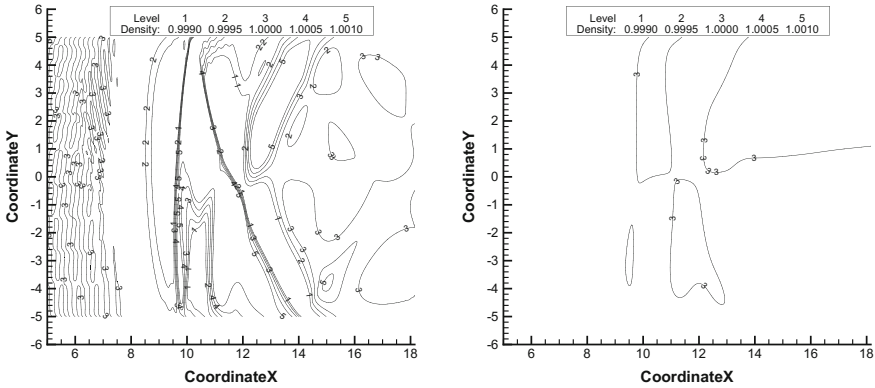
Fig. 9 Density contours at $t = 74$. *Left* without zonal BC, *Right* with adaptive sponge zone
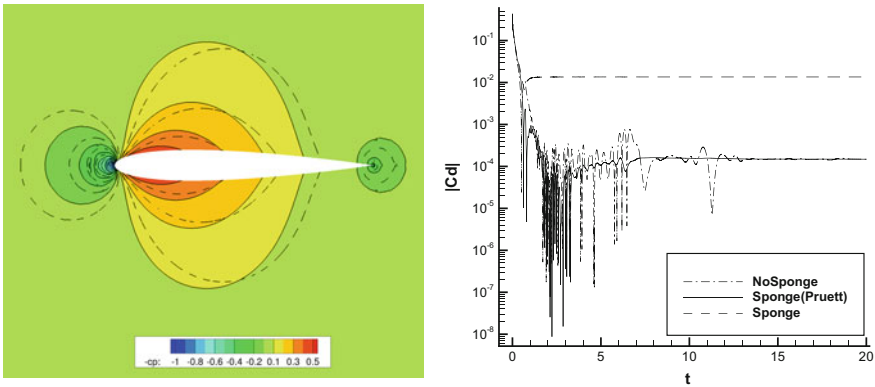
Fig. 10 *Left*: c_p contours: no sponge (*colors*), Pruett sponge (*solid lines*), sponge (*dashed lines*), *Right*: c_d convergence

sensitivity with regards to the sponge zone parameters and thus removes a source of computational uncertainty. To demonstrate this feature of the adjusting base flow, Fig. 10 (left) shows the results of a 2D Euler flow simulation at $Ma = 0.4$ around a NACA 0012 airfoil. Three simulation results are compared: (1) One without any sponge zone, one with a constant sponge (2) and one with the adjusting one (3), both applied in the entire field. The damping parameter is set to $d = 0.1$ and the filter width is 0.5 convective times (c/u_∞). Solution (1) and (3) show an identical flow field, while the classical sponge (2) clearly influences the steady state solution due to the base flow inconsistency. The right pane of Fig. 10 shows the convergence of the drag coefficient, which differs from the unfiltered results for case (2). Thus, the adjusting sponge zone can be implemented efficiently without a large memory requirement, it retains the steady state solution as it filters in time and it can be used to prevent reflections.

The full framework described in this section is available as the open-source code package FLEXI[1] under GPL 3.0.

4 Applications

In this section, we describe some CAA simulations with the DGSEM method presented in Sect. 3. We start by a brief presentation of a LEE sound scattering simulation to highlight the influence of the numerical scheme in terms of the n_{ppw} criterion in Sect. 4.1. In Sect. 4.2, tonal noise generation at an airfoil is computed and compared to well-established results to validate the established framework. In Sect. 4.3, we present the simulation of a feedback mechanism in a complex automotive test case.

4.1 Linearized Euler Equations

While the framework presented in Sect. 3 is mainly intended for direct methods, implementing hyperbolic/parabolic systems of equations beyond the compressible Navier–Stokes equations is straight forward. For this investigation, the Linearized Euler Equations (LEE) have been implemented:

$$\frac{\partial \rho}{\partial t} + (\mathbf{v}_0 \cdot \nabla_x)\rho + \rho_0 \nabla_x \cdot \mathbf{v} + (\mathbf{v} \cdot \nabla_x)\rho_0 + \nabla_x \cdot \mathbf{v}_0 \rho = 0 \tag{34}$$

$$\frac{\partial \mathbf{v}}{\partial t} + (\mathbf{v}_0 \cdot \nabla_x)\mathbf{v} + \frac{1}{\rho_0}\nabla_x p + (\mathbf{v} \cdot \nabla_x)\mathbf{v}_0 + \frac{1}{\rho_0}(\mathbf{v}_0 \cdot \nabla_x)\mathbf{v}_0 \rho = 0 \tag{35}$$

$$\frac{\partial p}{\partial t} + (\mathbf{v}_0 \cdot \nabla_x)p + \gamma p_0 \nabla_x \cdot \mathbf{v} + (\mathbf{v} \cdot \nabla_x)p_0 + \gamma(\nabla_x \cdot \mathbf{v}_0)p = 0 \tag{36}$$

For a constant base state $U_0 = (\rho_0, u_0, v_0, w_0, p_0)$, they can written in conservative form as

$$U_t + \mathbf{A}\, U_x + \mathbf{B}\, U_y + \mathbf{C}\, U_z = S, \tag{37}$$

with the acoustic source term S and the matrices $\mathbf{A}, \mathbf{B}, \mathbf{C}$ depending on U_0 only. Following the test case description from the Second Computational Aeroacoustics Workshop on Benchmark Problems (Tam and Hardin 1997), the scattering of a point source on a cylindrical object of diameter $D = 1$ is investigated. The source term acts through periodical pressure and density disturbances and is given by

---

[1] www.flexi-project.org.
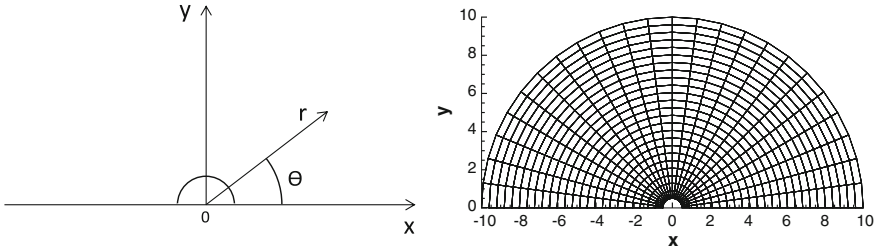
Fig. 11 Grid and coordinate system for LEE cylinder scattering test case

$$
S = \begin{pmatrix} \dfrac{\gamma}{c_0^2} S(x, y, t) \\ 0 \\ 0 \\ 0 \\ S(x, y, t) \end{pmatrix}, \quad S(x, y, t) = \exp\left[-ln(2) \frac{(x - x_c)^2 + (y - y_c)^2}{b^2} \right] \sin(\omega t),
$$

(38)

with $b = 0.2$, $\omega = 8\pi$, $\gamma = 1.4$ and the source coordinates $x_c = 4$ and $y_c = 0$. Initially, $U(t = 0) = 0$ and the background state is given by

$$
\rho_0 = 1, \mathbf{v}_0 = \mathbf{0}, p_0 = 0.714285714.
$$

(39)

The computational domain is a 2D half cylinder of radius $r = 10$, discretized by a structured grid with refinement towards the geometry. Symmetry boundary conditions are enforced on the lower boundary, while Dirichlet boundaries with vanishing fluctuations are enforced on the outer surface. Figure 11 depicts the geometry and grid as well as the coordinate system used. A number of computations have been conducted on different hierarchical grids and varying polynomial degree N. As a numerical flux function, a standard characteristic flux vector splitting was used. Figure 12 shows the instantaneous pressure and velocity fluctuations at $t = 100$.
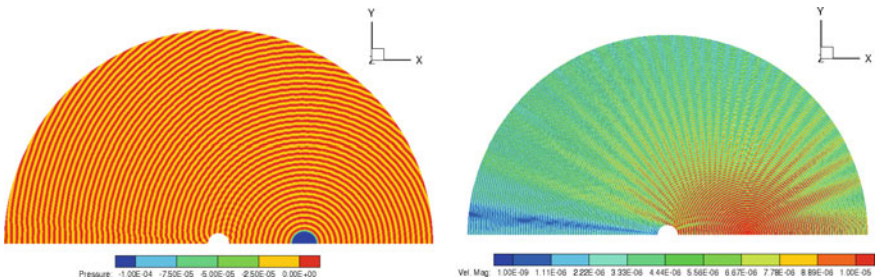
Fig. 12 Instantaneous pressure and velocity fluctuations at $t = 100$
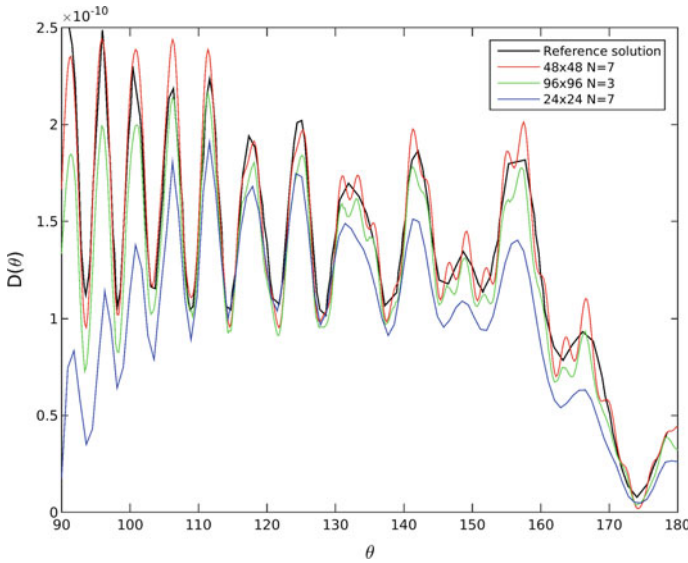
Fig. 13 Comparison of computed directivity with reference solution from Tam and Hardin (1997)

For a quantitative comparison, the directivity D as a function of the radius r can be computed from

$$D(\theta, r) = \overline{r p(\theta)^2}, \tag{40}$$

where the bar denotes the time-averaging. The averaging takes place between $t = 45$ and $t = 100$ once the initial disturbances have left the domain. Figure 13 compares the simulation results with analytical reference data. The simulations were conducted on three hierarchically refined structured grids with 24×24, 48×48 and 96×96 elements in the $x - y$-plane. The degree of the polynomial approximation was chosen to be $N = 3$ and $N = 7$. From the results in Fig. 13, two trends can be observed. Firstly, the solution improves towards the reference solution when the grid size is halved while keeping N constant. Secondly, the importance of a low n_{ppw} criterion is demonstrated here, as two simulations with the same overall number of DOF (96 elements, $N = 3$ and 48 elements, $N = 7$) differ significantly in accuracy. For this nominal resolution (taken along a 1D line at the lower boundary), the number of DOF per acoustic wavelength is ≈ 6. From the discussion in Sect. 2.2, this is less than optimal for accurate wave representation for an $N = 3$ approximation, but sufficient for $N = 7$. Accordingly, the $N = 7$ solution is in better agreement with the analytical reference. Figure 14 supports these observations. For the same total number of DOF, the high order solution (left) retains the acoustic waves up to the boundary, while for the low order solution (right), only the waves in close proximity to the source are kept intact.
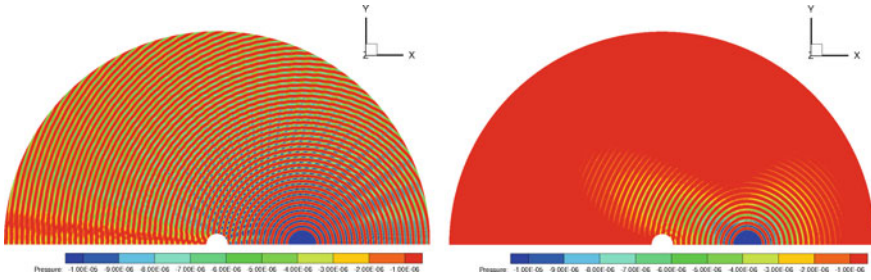
Fig. 14 Instantaneous pressure fluctuations at $t = 100$ with 384^2 DOF. *Left*: 48×48 elements, $N = 7$; *Right*: 192×192 elements, $N = 1$

4.2 NACA 0012 Tonal Noise

The DGSEM framework described in Sect. 3 has been applied to a number of turbulent and transitional test cases (Fechter et al. 2012; Flad et al. 2014; Beck et al. 2016, 2014) covering laminar separation, transition and turbulent reattachment in an LES setting. In the following, we will discuss the simulation of the flow around a NACA 0012 airfoil which has been shown to support the establishment of an acoustic feedback loop (Paterson et al. 1973; Arbey and Bataille 1983; Nash et al. 1999; Desquesnes et al. 2007; Jones and Sandberg 2011; Plogmann et al. 2013). We follow the 2D DNS of Jones and Sandberg (2011) and conduct a well-resolved simulation at $Ma = 0.4$ and $Re_C = 100,000$ based on the chord C at an angle of attack of $\alpha = 0°$.

The 2D domain is discretized in a C-type topology. The upstream radius is $r = 7C$, and extends to $9C$ downstream. The domain is divided into 40,934 unstructured elements, each supporting a polynomial of degree $N = 5$ per direction. This results in about 1.5 million degrees of freedom. The boundary geometry is represented by a polynomial of degree $N_{\text{geo}} = 4$ per direction. This ensures proper representation of the airfoil curvature. Details on the near-wall resolution of the current and the reference simulation from Jones and Sandberg (2011) are listed in Table 2. The far-field boundary conditions are enforced weakly, with a Roe Riemann flux function to enable the exiting of low amplitude waves as discussed in Sect. 3.4. In addition, a circular moving-average sponge zone is arranged around the trailing edge, with its

Table 2 Wall-tangential and wall-normal grid spacing Δx and Δy at the leading edge (LE) and trailing edge (TE) for the current simulation of the NACA 0012 case and reference Jones and Sandberg (2011). $\Delta x = \Delta x_{\text{Elem}}/(N + 1)$, $\Delta y = \Delta y_{Elem}/(N + 1)$

|	LE current	LE ref.	TE current	TE ref.
$\Delta x/C$	$4.2 \cdot 10^{-4}$	$6.1 \cdot 10^{-4}$	$5.3 \cdot 10^{-4}$	$4.0 \cdot 10^{-4}$
$\Delta y/C$	$2.3 \cdot 10^{-4}$	$3.5 \cdot 10^{-4}$	$2.3 \cdot 10^{-4}$	$4.0 \cdot 10^{-4}$
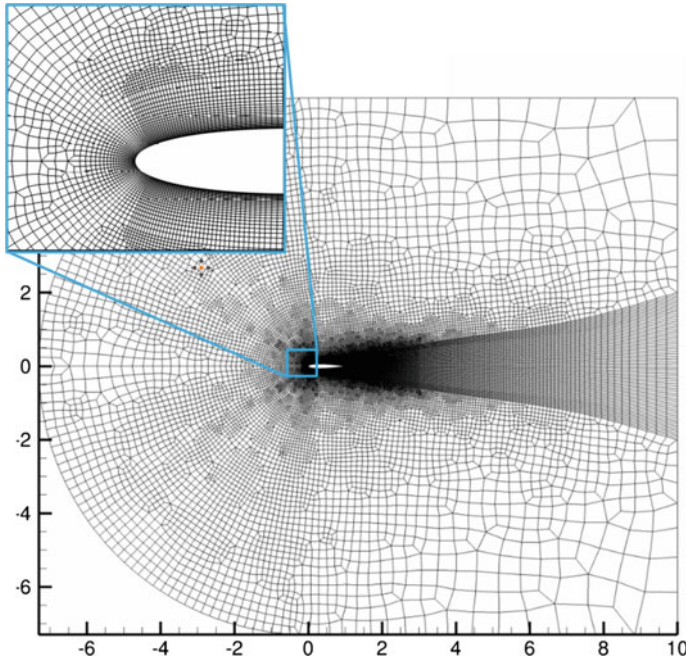
Fig. 15 Domain and grid for the NACA 0012 simulation

source term strength $d\sigma(\vec{x})$ ramped from 0 to 0.5 in the range $r/C = 2$ to 6, while the temporal filter width is set to $\Delta = 2C/u_\infty$. Figure 15 shows the domain and the grid. The simulation was conducted on the CRAY XC40 Hornet cluster using 720 cores, which resulted in a load of $\approx$2000 DOF/core, which is near the optimum of the framework. The resulting computational wall time amounted to 3 min per convective time unit $T^* = C/u_\infty$ at a time step of $\Delta t/T^* = 3.1 \cdot 10^{-5}$.

The general flow features are illustrated by instantaneous vorticity contours in Fig. 16 (left). The boundary layer separates on both sides of the airfoil, which leads to a roll-up of vortices slightly upstream of the trailing edge. Figure 16 (right) shows the associated acoustic radiation by means of volume dilatation $(\vec{\nabla}_x \cdot \vec{v})$ contours. The typical dipole character of trailing edge noise can be easily recognized.

The acoustic signal at an observer position of $0.5C$ above the airfoil can be compared to the reference in Fig. 17 by means of the PSD of pressure. The PSD is approximated by averaging over 5 blocks with 50% overlap and a Hanning window over a total of $36T^*$. The main tonal frequency and the overall shape of the decaying broadband noise are in excellent agreement. Deviations are found in the missing side peak at $fT^* \approx 3.3$ and additional lower side peaks at $fT^* \approx 2$ and 2.9 yielded by the present simulation, which do not appear in the reference.

In order to determine whether the underlying feedback mechanism is present and detected by the numerical simulation, a global stability analysis is conducted. More
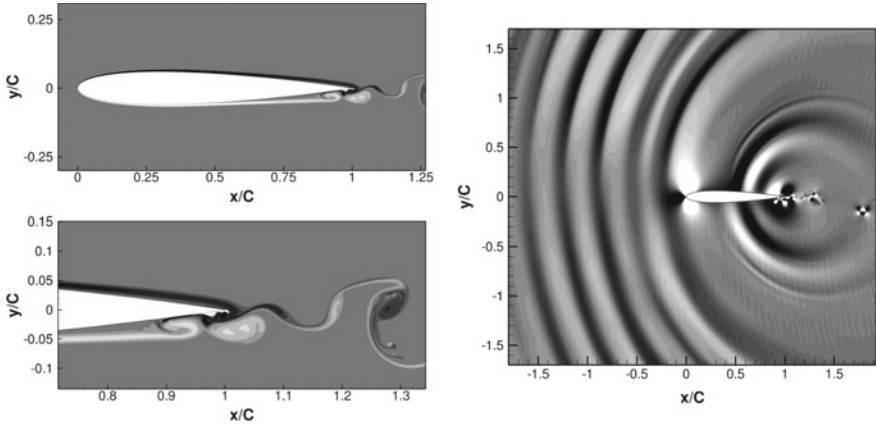
Fig. 16 *Left*: instantaneous vorticity contours over the range $\Omega_z = \pm 100 u_\infty/C$, *Right*: volume dilatation contours in the range $\vec{\nabla}_x \cdot \vec{v} = \pm 0.1 u_\infty/C$
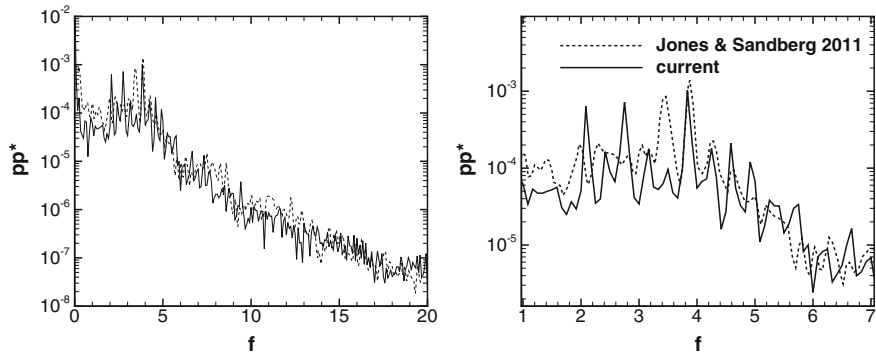

Fig. 17 PSD of pressure at $\vec{x}/C = (0.5, 0.5)$, where the origin is placed at the leading edge of the airfoil

details on this method can be found in Frank and Munz (2016). The basic concept of this type of analysis is to consider the temporal evolution of small disturbances on a frozen base flow. To this end, the solution U is rewritten as a Reynolds decomposition of the form $U = U_0 + U'$, where $(U_0)_t \neq 0$ for a general base flow. Introducing this ansatz into the evolution equation leads to an expression for the dynamics of small perturbations to arbitrary base flows:

$$U'_t = R(U_0 + U') - R(U_0). \tag{41}$$

This simple perturbation formulation is suitable for any non-linear solver, as it just requires the subtraction of the operator evaluated at the base state at every instance. A Taylor series expansion of the full evolution equation about U_0 shows that Eq. (41) approximates a linearization for small U'.
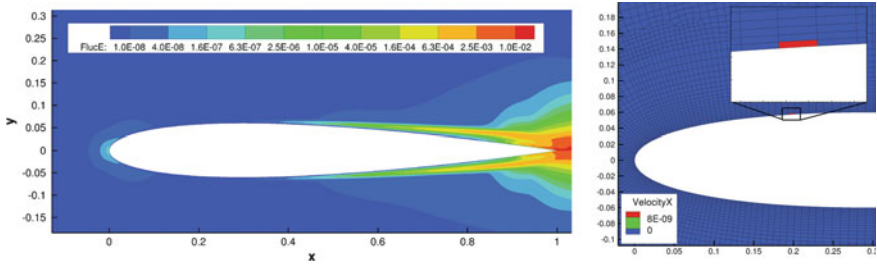
Fig. 18 *Left*: RMS fluctuations of velocities $\sqrt{\overline{u'u'} + \overline{v'v'}}$ for NACA 0012. *Right*: location of perturbation

For the present analysis, we chose the time-averaged base flow as U_0. It was then initially perturbed by a cell-constant value of $U'(t = 0)/U_\infty = 10^{-8}$ and left to evolve according to Eq. (41).

Figures 19 and 20 visualizes the feedback loop as an interplay of hydrodynamic instabilities (visualized by the vorticity in the left column) and the acoustic field (shown is the dilatation in the right column). Starting from the top, the perturbation was introduced at time $t = 0$ at the location shown in Fig. 18 (right). The perturbation is convected along the airfoil and grows in amplitude in the separated shear layer (t_1 in Fig. 19). As it passes the trailing edge, large scale acoustic radiation is generated and propagates (also) upstream (t_2). At t_3, the energetic part of the wave package has left the trailing edge, and the associated acoustic radiation subsides, leading to a visually "quiet" state again (t_4 in Fig. 20). Some time later, although no further perturbation has been introduced externally, a new energetic wave package appears (t_5), which again generates acoustics upon shedding (t_6), thereby closing the loop.

This simulation of the feedback loop and comparison with published results serves as a validation case for our framework. The accurate prediction of the acoustic signal and the establishment of the feedback loop are only possible if the precise hydrodynamic and acoustic processes are captured by the simulation. The close agreement of our simulation with the acoustic results of the reference demonstrate the suitability of our high order code framework for aeroacoustic feedback effects. In the following, it will be applied to a more complex case of acoustic feedback at an automotive side mirror.

### 4.3   Acoustic Feedback Mechanism at a Side Mirror

Feedback as a source of tonal noise In this section, we will present the application of the framework to a complex acoustic problem in an industrial setting, namely the tonal noise generated by an acoustic feedback loop on a car side mirror alongside experimental data. The numerical results presented in here are based on the work by Frank (2016), while the joint experimental analysis was conducted by Werner (2017).
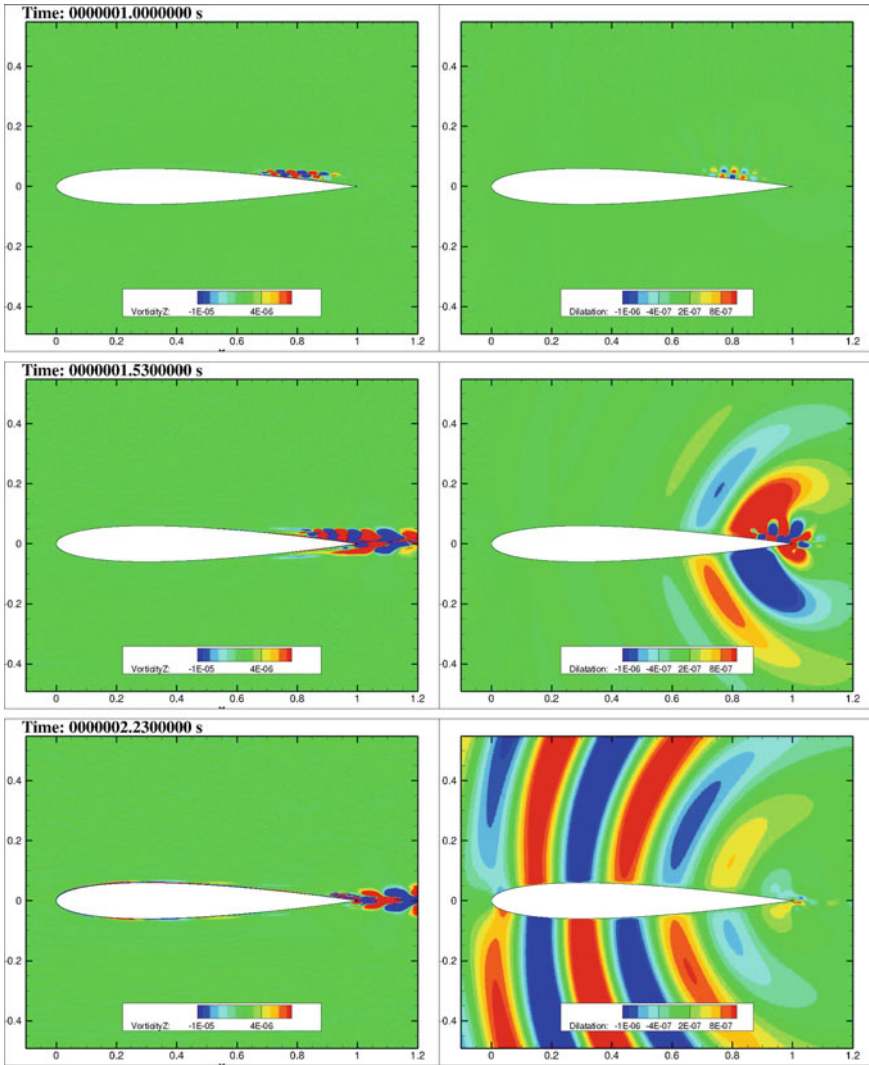
Fig. 19 Part A: temporal evolution of z-vorticity and dilatation rate for NACA 0012 case, each row corresponds to an instance in time t_i, $i = 1, \ldots, 3$. (See also Fig. 20)

Aerodynamically, typical mirror shapes can be classified as bluff-body configurations, with the associated flow phenomena. As observed experimentally, the mirror is known to be a source of tonal noise. The associated narrowband amplitude peaks in the acoustic spectrum are typically perceived as disturbing whistling sounds. The main method of research into their origins for the mirror configuration remains experimental, and is limited to simplified mirror geometries for numerical studies. The only simulation of a realistic mirror known to the authors was reported by
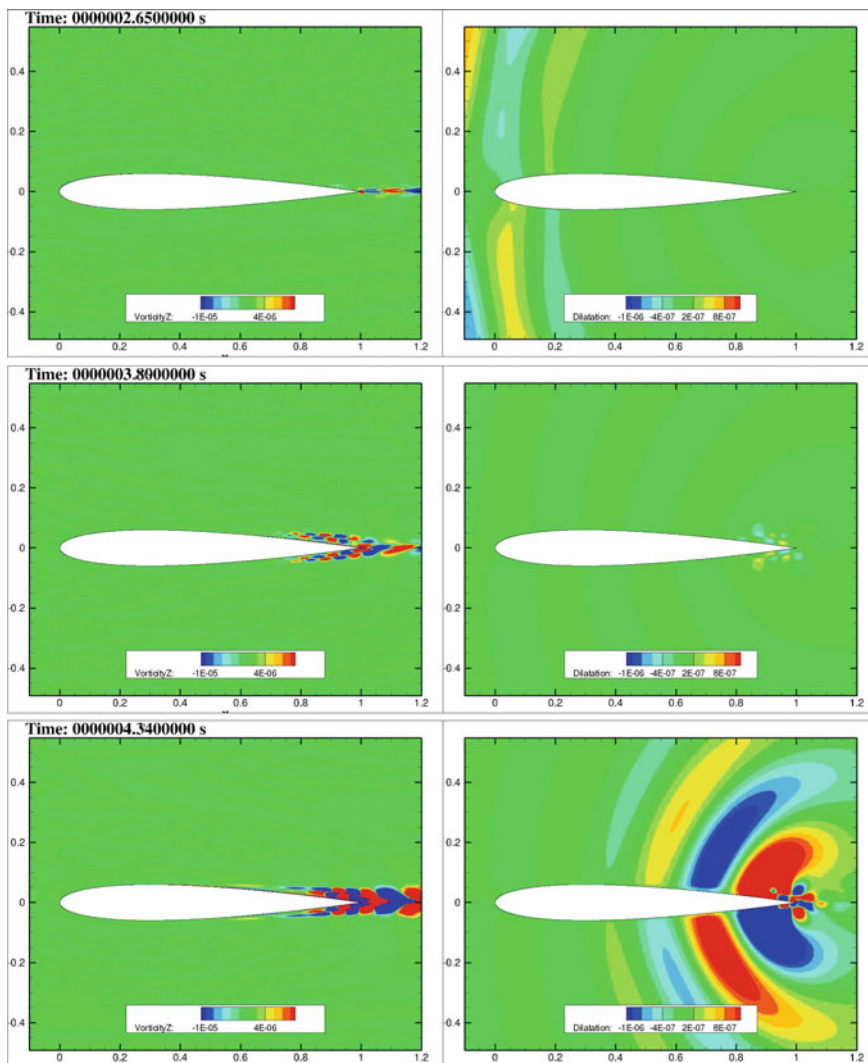
Fig. 20 Part B: temporal evolution of *z*-vorticity and dilatation rate for NACA 0012 case, each row corresponds to an instance in time t_i, $i = 4, \ldots, 6$. (See also Fig. 19)

Khalighi et al. (2010). For more generic geometries like airfoils however, a number of numerical simulations of self-noise exist, e.g. Jones and Sandberg (2010), Desquesnes et al. (2007), Chong and Joseph (2012), see also the computation presented in Sect. 4.2. Lounsberry suggested that a similar feedback mechanism as the one found on airfoils was responsible for the noise generation along car mirrors, noting the shared occurrence of attached laminar or transitional boundary layers up until close to the trailing edge (Lounsberry et al. 2007).
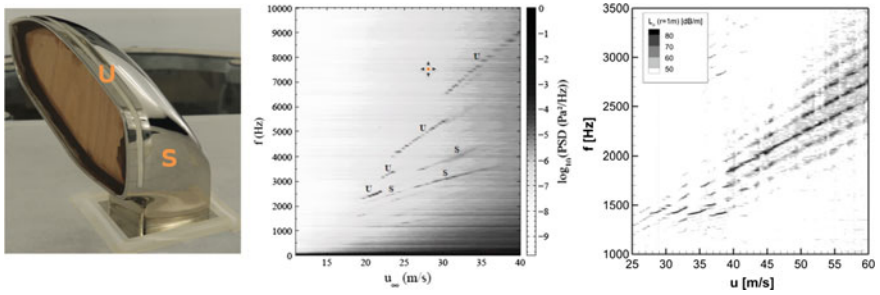
Fig. 21 *Left*: model mirror on wind tunnel floor from Werner et al. (2017a), *Middle* acoustic measurements on mirror, from Werner et al. (2017b), *Right*: acoustic measurements on NACA 0012 airfoil, from Plogmann et al. (2013)

While tonal noise at airfoils has been observed both experimentally e.g. Arbey and Bataille (1983), Plogmann et al. (2013), Paterson et al. (1973) as well as numerically, different theories about the exact mechanism exist. Paterson et al. (1973) attributed the noise to the bluff-body vortex shedding with a distinct Strouhal frequency at the trailing edge. However, this explanation did not account for the ladder-type structure observed when plotting the tonal frequency over the freestream velocity, i.e. the distinct jumps in frequency, see Fig. 21. Several other models have been proposed, which are based on the concept that for a self-sustaining feedback loop, the phase difference over one cycle should vanish, a condition that only discrete frequencies can fulfill (Tam 1974; Kingan and Pearse 2009; Arbey and Bataille 1983). Using receptivity strips at different locations in the laminar boundary layer along a NACA 0012 airfoil, Plogmann et al. were able to trigger receptivity experimentally, which resulted in a change of the tonal frequency according to the phase criterion, strongly supporting the notion of acoustic feedback as an explanation for the frequency selection.

Figure 21 (left) shows the mirror model on the floor of the Laminar Wind Tunnel at the Institute of Aerodynamics and Gasdynamics (IAG). The measured frequency spectra as a function of freestream velocity u_∞ are shown alongside (middle plot). The ladder structure is visible both for the side and upper surfaces. Through boundary layer tripping, the regions of tonal noise generation could be established. For comparison, the right plot depicts similar measurements for a NACA 0012 airfoil.

In Fig. 22, the building blocks of the feedback loop are shown: A laminar boundary layer along a convex geometry separates close to the trailing edge due to the adverse

**Fig. 22** Conceptual model for the feedback loop
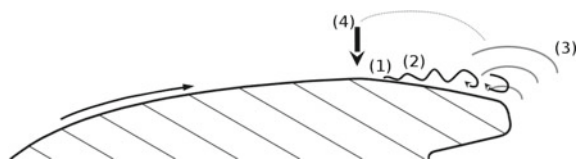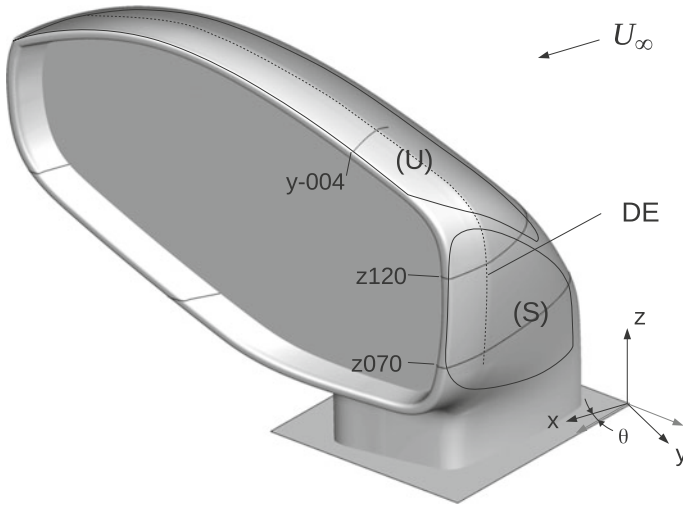
Fig. 23 Mirror geometry. Marked areas are *S* Side surface, *U* Upper surface, *DE* Design edge

pressure gradient (1). In the resulting detached shear layer, convective instabilities are amplified and start the roll-up into coherent vortices (2). When passing the trailing edge, these structures generate sound waves through scattering (3). Pressure waves run upstream through the boundary layer and reinforce the boundary layer instability due to receptivity, thereby closing the loop (4). This is essentially the same mechanism as presented in Sect. 4.2.

Numerical Model As confirmed by the experimental investigation of Werner et al., the non-generic early-development-stage side-view mirror depicted in Fig. 21 develops a distinct whistling sound at normal cruise speeds, provided that the inflow turbulence level is kept low (Werner 2017). Figure 23 shows the computational model of this mirror geometry and the coordinate system. To enable direct comparison with the experimental data, an isolated mirror was considered. The length scale $L = 0.1$ m corresponds to the lateral length of the side surface. The free-stream velocity was set to 100 km/h, and a yaw angle of $\theta = -20°$ was chosen. This angle resulted from a preliminary investigation, in which it was found that this yaw angle resulted in a comparable pressure distribution on the mirror side surface, when compared to a full configuration with the mirror mounted on the car chassis. As the mirror side and upper surface are outside the wind tunnel boundary layer (Frank 2016), no influence of the wind tunnel boundary layer on the tonal noise generation is expected. Therefore, symmetry boundary condition are applied on the wind tunnel floor, while the free-stream boundary conditions are chosen as weakly enforced Dirichlet conditions, see Sect. 3.4. On the mirror geometry, isothermal wall boundary conditions are applied. A temporally adapting sponge zone is added upstream of the outflow boundary. The associated source term is ramped parallel to the free-stream velocity vector beginning at approximately $2L$ downstream of the average trailing edge of the mirror. Based
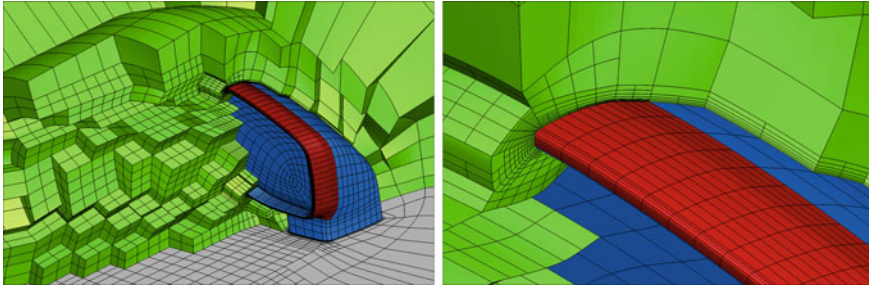
Fig. 24 Cut view of the computational mesh close to the mirror, showing the non-conforming interfaces

on the time scale $T = L/u_\infty$, the damping parameter and the temporal filter width are set to $d = 0.8/T$ and $\Delta = 4T$, respectively.

The computational mesh is created in two-step process. First, a coarse, block-structured grid made of hexahedral cells is generated with a commercial grid generator. Afterwards, this mesh is refined in user-specified regions by isotropic cell splitting, namely in the boundary layer around the mirror and in the wake region up to the outflow boundary. This introduces non-conforming cell interfaces. A second refinement level is introduced on the trailing edge area, in which the feedback process outlined in Fig. 22 is known to occur from the experiments. This area is marked in red in Fig. 24. The refinement is managed by the software library p4est (Burstedde et al. 2011), the resulting mesh consisted of 32,800 elements. The curved surface of the mirror is realized via an agglomeration approach (Hindenlang et al. 2015). The mapping from reference to physical space is constructed from a super-sampled version of the unrefined base grid. For the refined cells, the mapping can simply be evaluated in the respective subset of the lower level parameter space. This way, we ensure free stream preservation and conservation also at the non-conforming interfaces.

Simulation Results

Spatial resolution To assess the influence of the spatial resolution on the results, a p-refinement is conducted by increasing the local polynomial degree. This not only increases the number of degrees of freedom, but also shifts the n_{ppw} factor due to the increase in the approximation order. Two resolutions are considered: Case $N4M6$ denotes an approximation of degree $N = 4$, with an evaluation of the non-linear inner products with an approximation of degree $M = 6$. Analogously, case $N7M10$ denotes an approximation of degree $N = 7$. Details on the de-aliasing approach can be found in Beck (2015). The resulting mesh parameters are listed in Table 3.

Table 3 Computational mesh and resolution details

| Case	DOF	Δt [s]	Δy [mm]	Δy^+	Δx [mm]	Δx^+
N4M6	$4.1 \cdot 10^6$	$3.9 \cdot 10^{-8}$	0.026	2.5	0.6	80
N7M10	$16.8 \cdot 10^6$	$1.8 \cdot 10^{-8}$	0.016	1.5	0.38	40
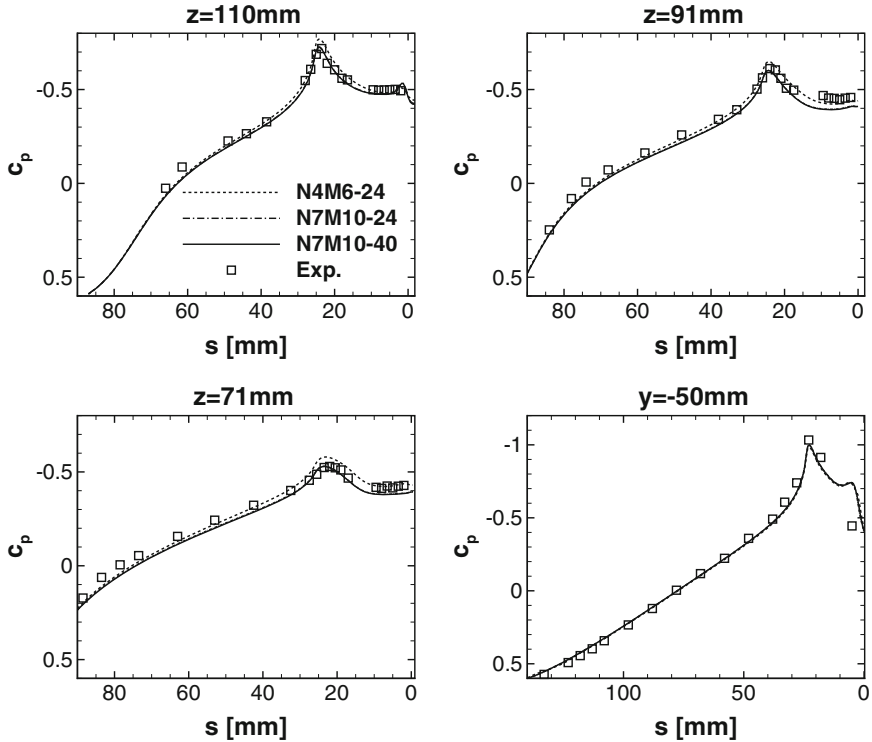
Fig. 25 Computational and measured pressure coefficient distributions along surface lines $z = 110$, $z = 71$ and $y = -100$ mm. s denotes the wall-tangential distance to the trailing edge

The wall-normal and wall-tangential grid spacings Δy and Δx are given with respect to the inner-element resolution, which takes the degrees of freedom within each cell into account: $\Delta y = \Delta y_{Element}/(N + 1)$. They represent maximum values in the refined region on the side surface. All simulations were conducted on the CRAY XC40 Hornet cluster at HLRS. The wall time per convective time $T^* = L/u_\infty$ on 3288 cores for simulations $N7M10$ and $N4M6$ amounted to about 4.6 and 0.6 h, respectively.

Figure 25 compares the time-averaged surface pressure coefficient for the two resolutions. The pressure coefficient is extracted along lines with $z = $ const. on the side surface and $y = $ const. on the upper surface. Experimental data from Werner et al. (2017a) is given for comparison. Additionally, for the case $N7M10$, two averaging periods (24 and 40 T^*) are compared. The results for the different averaging windows are not discernible, suggesting that the chosen time frames are sufficient and a statistically steady mean flow is reached. With regards to the p-refinement, it should be noted that the resolution for case $N7M10$ corresponds nearly to an isotropic doubling of the resolution, even without taking the more accurate approximation into account. Thus, the slight difference between the two resolution indicates that a

Fig. 26 Isocontours of the time-averaged pressure coefficient and surface streamlines based on wall friction
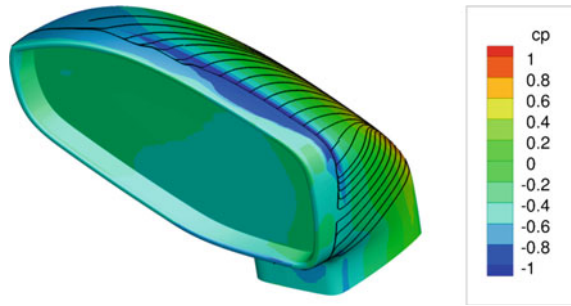
regime of weak grid dependence is reached. Based on these findings and taking into account the close agreement with the experimental static pressure measurements, the following analysis focuses on the highest resolution case.

Time-Averaged Flow Field The time-averaged flow field is characterized by the pressure coefficient on the mirror surface. Figure 26 shows the corresponding c_p distribution as well as the surface streamlines based on the skin friction on the leeward side. About 25 mm upstream of the trailing edge, shortly downstream of the design edge (marked "DE" in Fig. 23), the coalescing skin friction lines indicate a boundary layer separation, supported also by the increase in pressure along the trailing edge.

From the experiments, one possible source of tonal noise has been located at the side surface. To quantify the boundary layer in that area, a Particle Image Velocimetry (PIV) measurement campaign was conducted at the $z = 110$ mm position (see Fig. 23). The PIV data is plotted alongside the results from the numerical simulation. Figure 27 (left and right) shows contour plots of the time-averaged velocity magnitude and root mean square (RMS) velocity fluctuations. Overall, LES and PIV
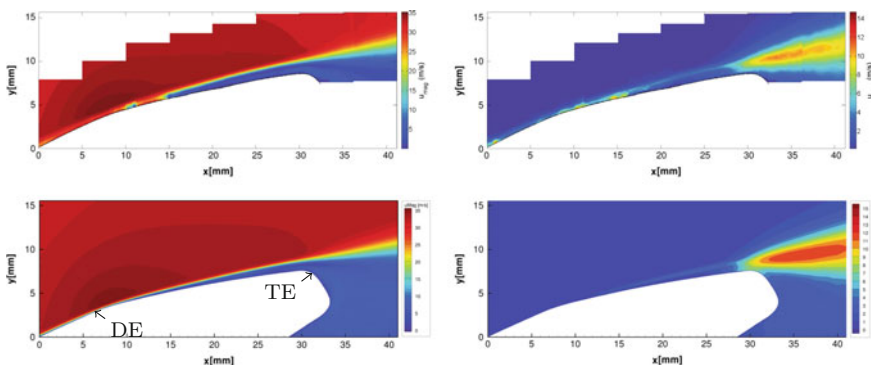

Fig. 27 Comparison of the simulation results (*bottom*) with PIV data (*top*) in the $z = 110$ mm plane. *Left* time-averaged velocity magnitude $\langle \vec{v} \cdot \vec{v} \rangle^{1/2}$, *Right* RMS velocity fluctuations $\langle \vec{v}' \cdot \vec{v}' \rangle^{1/2}$. The origin of the coordinate system in this plot is arbitrarily shifted to match the PIV data

data are in good agreement. The point of separation is predicted by the LES shortly downstream of the design edge in both cases, while the experimental data shows some artifacts in that region which can be attributed to seeding material deposition between the measured slice and the camera. The spreading rate of the shear layer and its separation angle are in very close agreement. From the RMS fluctuations, it can be determined that the flow remains laminar and steady through the separation up to the trailing edge, where the region of large amplitude fluctuations begins.

Acoustic Field and Source Identification Based on the comparisons of the hydro-dynamic flow field with experimental data in the previous section, the focus is now shifted towards the acoustic emissions and source locations, with a focus on the occurrence and description of tonal noise. During the simulation, the local pressure signal is recorded at a rate of 44.1 kHz over $45T^*$ at 4000 position along a circular array of radius $r = 500$ mm. From this data, the PSD is computed using blocks with 2048 samples and 50% overlap. To reduce spectral leakage for non-periodic signals, a Hanning window is used.

A visual impression of the spatial distribution of the acoustic field is given in Fig. 28. Contours of the sound pressure level (SPL) of selected frequencies and the
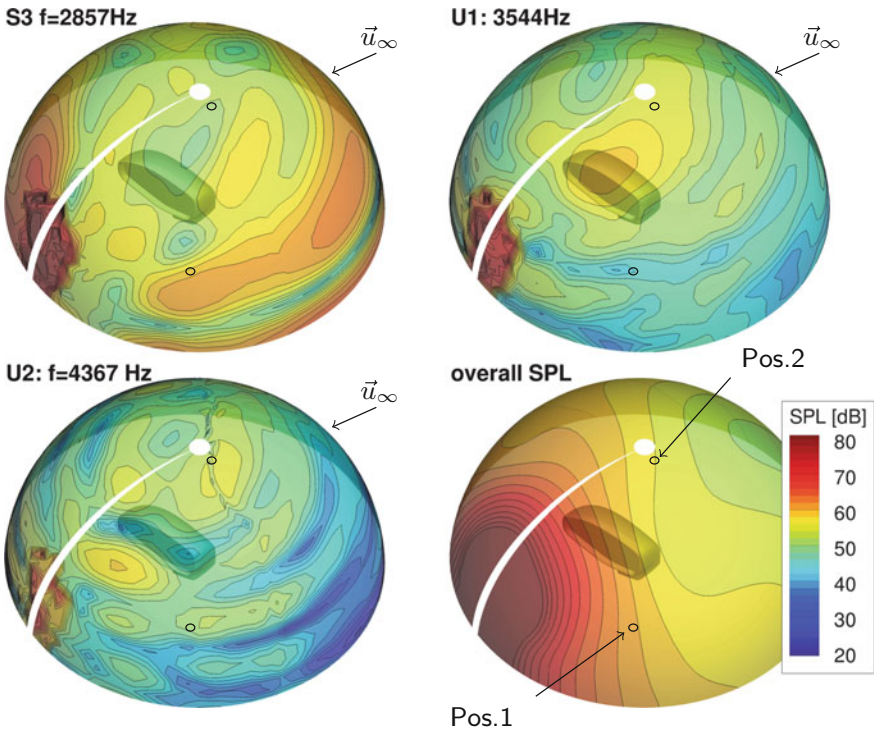
Fig. 28 SPL for selected frequencies and overall SPL (*bottom right*) on a spherical evaluation surface of $r = 500$ mm placed around the mirror
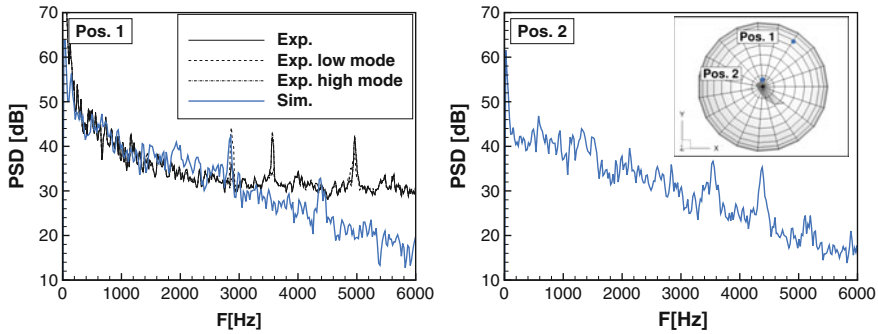
Fig. 29 PSD of pressure at two representative positions outside of the unsteady hydrodynamic field. PSD reference value: $4 \cdot 10^{-10} \, \text{Pa}^2/\text{Hz}$. The inset in the right panel shows the probe positions relative to the mirror geometry

overall SPL are plotted on a half-sphere above the mirror. As expected, the overall SPL increases significantly downstream of the mirror, due to the primary location of the noise sources at the leeward side of the mirror and the upstream shielding effects. Also, the exiting turbulent wake represents a strong source of noise. The acoustic footprint of the wake manifests itself as a "loud" spot across all selected frequencies. For each chosen frequency, a complex spatial wave pattern can be observed. For $f = 2857 \, \text{Hz}$, a strong lateral radiation can be observed, which also extends upstream. For $f = 3544$ and $4367 \, \text{Hz}$, more focused noise spots above and downstream of the mirror can be observed. Based on this qualitative analysis, we can expect that the frequency spectra vary significantly with the probe position. Therefore, the power spectral densities (PSD) of pressure in Fig. 29 are plotted at two representative probe positions, aiming at capturing the acoustic emission from the side surface at Pos. 1 and those from the upper surface at Pos. 2. The probes are located on a sphere with $r = 500 \, \text{mm}$ around the mirror, their positions are depicted in the right panel. The vertical positions are $z = 270$ and $z = 500 \, \text{mm}$ above the bottom wall for Pos. 1 and Pos. 2, respectively. The left panel includes inflow microphone measurements.

Before discussing the results, some remarks on the experimental setup and the comparability are necessary, which might help explain the results below. While in the simulation, a perfect free stream around the mirror is chosen, the experiments were conducted in a closed, rectangular test section. The scattering on the enclosure walls thus can be expected to influence the acoustic measurements. In addition to these effects, the transition locations and turbulence intensities in the parts of the flow around the mirror emitting the relevant broadband components cannot be guaranteed to match experimental ones, since the inflow turbulence level was not considered. Finally, the background noise of the wind tunnel is not captured in the simulation. Therefore, the following quantitative comparison focuses on the tonal noise frequencies, while the broadband noise spectra or amplitudes cannot be expected to match. Thus, the goal is the detection and comparison of the tonal components.

At Pos. 1, the simulated acoustic spectrum is composed of an evenly decaying broadband part and two recognizable, focused peaks at around 2860 Hz (S3) and 4380 Hz (U2). The first peak corresponds very well with the one found at 2900 Hz radiating from the mirror side during the experiments. However, an additional peak at 3500 Hz was also observed experimentally. A closer analysis revealed that the two modes alternated intermittently in an irregular fashion. Essentially, only one of them was noticeable at a given instant. The experimental spectrum is thus the result of averaging about the associated periods. Therefore, two additional experimental spectra corresponding to the low and high modes gained with conditional averaging are included in the plot. The simulation apparently predicts a situation where the lower of the two modes is favored. A switching of the modes was not observed numerically. While the precise reason for the alternation in the experiment is unknown, the switching between the two regimes triggered by loudspeaker forcing was shown in Werner et al. (2017b), indicating a high sensitivity to environmental disturbances of the flow in the experimental setup. Since the simulation setup is controlled and fixed, it is conceivable that the switching does not occur without voluntary triggering. In addition, due to the finite computational resources, the averaging time was significantly shorter than the observed alternation periods.

At Pos. 2, the computational data exhibits two tones at 3550 Hz (U1) and 4380 Hz (U2), which originate at the upper surface. The latter tone is also observed at Pos. 1, while the first is not, which can be explained by referring to Fig. 28: Pos. 1 lies within a shadowed region regarding the acoustic propagation of U1. The experimental spectrum at Pos. 1 only exhibits a single peak radiated from the upper surface, which has a significantly higher frequency of about 5000 Hz (Fig. 29 (left)). An indication for a tone of a similar frequency in the simulation is found in the weak trace of a peak at about 5000 Hz in the computational data at Pos. 2, which is generated at the upper surface.

In order to locate the dominant noise sources, an experimental beam-forming with a linear microphone array was conducted. Results indicate that the main source regions are located around the airfoil trailing edge, analogously to airfoil self-noise. Therefore, in Fig. 30, the spectra of wall pressure fluctuations along the trailing edge are plotted. The local coordinate r traverses the trailing edge from the lower side surface to the outer top surface. The side and upper portion are marked in Fig. 30. The PSD spectra are calculated using using blocks of 1024 samples averaged over $28T^*$. On both the side and the upper surface, two areas are marked that contain clear narrowband frequency peaks. Specifically, the side surface features the expected peak at approx. 2860 Hz corresponding to S3, while on the upper surface multiple additional narrowband features are visible. Among these features we recognize U1, U2 and the weak trace at 5000 Hz. Thus, each tone observed in the acoustic spectra has a counterpart in the wall pressure spectrum. The various tonal noise components therefore originate from the respective hydrodynamic fluctuations at the trailing edge.

Unsteady Flow Field In the previous section, the wall pressure fluctuations were connected to the generation of tonal noise. In order to characterize the underlying unsteady hydrodynamic field, its instantaneous vortical structures are visualized in
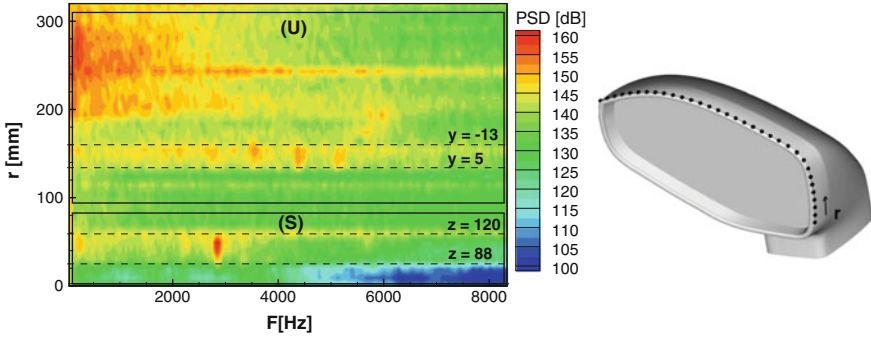
Fig. 30 Power spectral density of the wall pressure along the circumferential coordinate r at the trailing edge. PSD reference value: $4 \cdot 10^{-10}/\text{Pa}^2\,\text{Hz}$
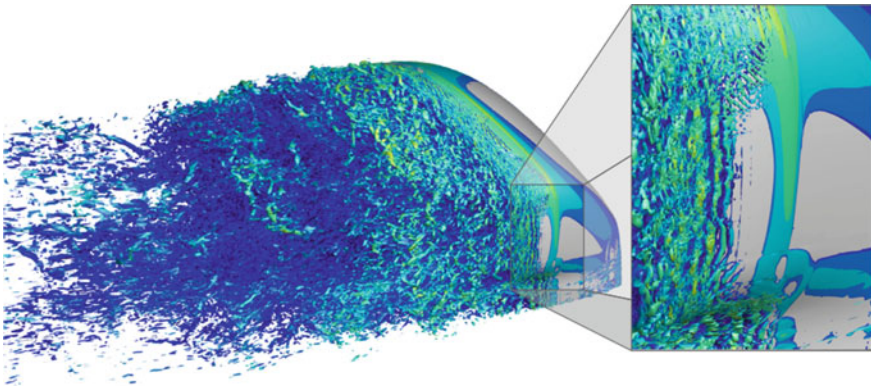
Fig. 31 Vortical structures at a flow field snapshot visualized by isosurfaces of $Q = 100(u_\infty/L)^2$ colored with velocity magnitude

Fig. 31 by the means of isosurfaces of the Q-criterion (Haller 2005), colored by velocity magnitude.

The initial laminar flow appears as a smooth surface on the front side of the mirror. The first vortical structures appear between the design edge and the trailing edge. On the side surface, a regular pattern of spanwise oriented rollers emerge. To evaluate the frequency associated with these coherent structures, which are a clear candidate for the development of tonal noise, a discrete temporal Fourier transform is performed. Details on the specific analysis can be found in Frank and Munz (2016), Frank (2016) and strongly support the notion that the tone associated with the side surface S3 originates from the passing of these structures over the trailing edge. A visual impression of the associated spatial structures is given in Fig. 32, where tonal mode S3 is compared to two representative modes of the surrounding broadband range. Shown are the isosurfaces of streamwise velocity fluctuations in the top row, and the isocontours of pressure fluctuations in the $z = 110\,\text{mm}$ cut in the bottom
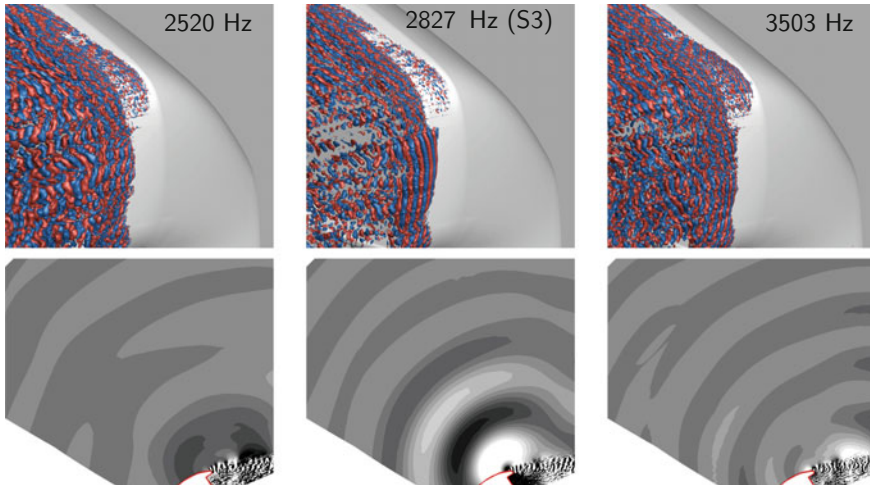
Fig. 32 *Top* isosurfaces of (the real part of) positive and negative velocity in the streamwise direction. The levels are chosen to ensure comparability. *Bottom* pressure contours at $z = 110$ mm. The *left*, *middle* and *right columns* correspond to $f = 2520$, 2827 and 3503 Hz

row. Note that plotting the real part results in an arbitrary but spatially consistent phase. The isosurfaces of S3 exhibit clear ordered coherent structures on the side surface, and the associated acoustic field indicates a high amplitude tonal source in the direct vicinity of the trailing edge. For the other two frequencies, such clear levels of coherence cannot be identified, and no clear statement regarding the source position can be made.

In summary, in this section we have demonstrated how the DGSEM framework can be used successfully in the direct noise computation in challenging domains. We have shown a near perfect comparison of the hydrodynamic field to the experimental data, and a very close agreement between the simulated and measured emitted noise frequencies. A global stability analysis similar to the one presented in Sect. 4.2 was conducted which confirmed the existence of the feedback loop and showed very good agreement of the loop frequency with the phase condition. Further details can be found in Frank and Munz (2016). To the authors' knowledge, this constitutes the first numerical simulation of the tonal feedback mechanism at a three-dimensional, complex geometry.

5 Conclusion

In this chapter, we have given an overview of the state of the art of direct acoustic simulation with Discontinuous Galerkin methods. Many variants of DG methods exist, which mainly differ in implementation details, meshing flexibility and

computational efficiency. However, they all share the basic advantages of the method for DNS and DNC: They allow arbitrary order in space, which supports excellent wave propagation properties and thus reduces the number of degrees of freedom required to simultaneously resolve small scale fluctuations alongside large scale structures. Due to the inter-element numerical fluxes, they are also naturally suited for hyperbolic problems and thus are an attractive base scheme for multi-scale problems such as the acoustic noise generation and emission arising from the compressible Navier–Stokes equations. Since the boundary conditions can be enforced weakly through characteristic-splitting based flux functions, far-field acoustic boundary conditions can be applied in a straight-forward manner. For the outflow boundary, where large amplitude nonlinear structures exit, an absorbing layer approach is feasible. We have presented such a sponge zone approach based on an adaptive, temporally filtered base flow, which has the advantage of preserving the time-averaged hydrodynamic flow field.

The framework FLEXI is based on a specific, highly efficient variant of the DG family. It has shown excellent scaling on high performance computing clusters for large scale simulations of turbulence. With the help of recent additions in terms of boundary conditions and analysis postprocessing tools, FLEXI has been extended towards challenging direct noise computations in complex domains. We have demonstrated the suitability of the framework for DNC, in particular for the exploratory numerical investigations into complex interactions of noise and flow such as the feedback mechanism. The numerical simulation of this mechanism, which has been identified as a main source of tonal noise around bluff bodies, demands a highly accurate numerical scheme for laminar, transitional and turbulent regions of the flow as well as a faithful resolution of the geometry. With the help of the DG methods, the numerical representation of this feedback mechanism at a complex automotive side mirror was possible for the first time.

References

Akervik, E., Brandt, L., Henningson, D. S., Hoepffner, J., Marxen, O., & Schlatter, P. (2006). Steady solutions of the Navier-Stokes equations by selective frequency damping. *Physics of Fluids*, *18*(6), 068102.

Arbey, H., & Bataille, J. (1983). Noise generated by airfoil profiles placed in a uniform laminar flow. *Journal of Fluid Mechanics*, *134*, 33–47. ISSN 1469-7645, 0022-1120.

Bassi, F., & Rebay, S. (1997). A high-order accurate discontinuous finite element method for the numerical solution of the compressible Navier-Stokes equations. *Journal of Computational Physics*, *131*(2), 267–279. ISSN 0021-9991.

Bazilevs, Y., & Hughes, T. J. R. (2007). Weak imposition of Dirichlet boundary conditions in fluid mechanics. *Computers and Fluids*, *36*(1), 12–26. ISSN 0045-7930.

Beck, A. (2015). High order discontinuous Galerkin methods for the simulation of multiscale problems. Ph.D. thesis, University of Stuttgart.

Beck, A. D., Bolemann, T., Flad, D., Frank, H., Gassner, G., Hindenlang, F., et al. (2014). High-order discontinuous Galerkin spectral element methods for transitional and turbulent flow simulations. *International Journal for Numerical Methods in Fluids*, *76*(8), 522–548.

Beck, A. D., Flad, D. G., Tonhäuser, C., Gassner, G., & Munz, C.-D. (2016). On the influence of polynomial de-aliasing on subgrid scale models. *Flow, Turbulence and Combustion*, 1–37.

Bogey, C., & Bailly, C. (2004). A family of low dispersive and low dissipative explicit schemes for flow and noise computations. *Journal of Computational Physics*, *194*(1), 194–214. ISSN 0021-9991.

Burstedde, C., Wilcox, L., & Ghattas, O. (2011). p4est: Scalable algorithms for parallel adaptive mesh refinement on forests of octrees. *SIAM Journal on Scientific Computing*, *33*(3), 1103–1133. ISSN 1064-8275.

Choi, H., & Moin, P. (2012). Grid-point requirements for large eddy simulation: Chapman's estimates revisited. *Physics of Fluids*, *24*, 011702–011702. ISSN 0899-8213.

Chong, T. P., & Joseph, P. (2012). Ladder-structure in tonal noise generated by laminar flow around an airfoil. *The Journal of the Acoustical Society of America*, *131*(6), EL461–EL467. ISSN 0001-4966.

Cockburn, B., & Shu, C.-W. (1989). TVB Runge-Kutta local projection discontinuous Galerkin finite element method for conservation laws II: General framework. *Mathematics of Computation*, *52*(186), 411–435. ISSN 0025-5718.

Cockburn, B., & Shu, C.-W. (1991). The Runge-Kutta local projection p1-discontinuous-Galerkin finite element method for scalar conservation laws. *ESAIM: Mathematical Modelling and Numerical Analysis*, *25*(3), 337–361. ISSN 0764-583X, 1290-3841.

Cockburn, B., Lin, S.-Y., & Shu, C.-W. (1989). TVB Runge-Kutta local projection discontinuous Galerkin finite element method for conservation laws III: One-dimensional systems. *Journal of Computational Physics*, *84*(1), 90–113. ISSN 0021-9991.

Cockburn, B., Hou, S., & Shu, C. W. (1990). The Runge-Kutta local projection discontinuous Galerkin finite element method for conservation laws. IV: The multidimensional case. *Mathematics of Computation*, *54*(190), 545–581. ISSN 0025-5718.

Collis, S. S. (2002). Discontinuous Galerkin methods for turbulence simulation. In *Proceedings of the 2002 Center for Turbulence Research Summer Program* (pp. 155–167).

Colonius, T. (2004). Modeling artificial boundary conditions for compressible flow. *Annual Review of Fluid Mechanics*, *36*, 315–345.

Colonius, T., & Lele, S. K. (2004). Computational aeroacoustics: Progress on nonlinear problems of sound generation. *Progress in Aerospace Sciences*, *40*(6), 345–416. ISSN 0376-0421.

Desquesnes, G., Terracol, M., & Sagaut, P. (2007). Numerical investigation of the tone noise mechanism over laminar airfoils. *Journal of Fluid Mechanics*, *591*, 155–182. ISSN 1469-7645, 0022-1120.

Fechter, S., Hindenlang, F., Frank, H., Munz, C.-D., & Gassner, G. (2012) Discontinuous Galerkin schemes for the direct numerical simulation of fluid flow and acoustics. In *18th AIAA/CEAS Aeroacoustics Conference (33rd AIAA Aeroacoustics Conference)*. American Institute of Aeronautics and Astronautics. doi:10.2514/6.2012-2187.

Flad, D., Beck, A. D., Gassner, G., & Munz, C.-D. (2014). A discontinuous Galerkin spectral element method for the direct numerical simulation of aeroacoustics. In *20th AIAA/CEAS Aeroacoustics Conference*. American Institute of Aeronautics and Astronautics. doi:10.2514/6.2014-2740.

Frank, H. M. (2016). High order large eddy simulation for the analysis of tonal noise generation via aeroacoustic feedback effects at a side mirror. Ph.D. thesis, University of Stuttgart.

Frank, H. M., & Munz, C.-D. (2016). Direct aeroacoustic simulation of acoustic feedback phenomena on a side-view mirror. *Journal of Sound and Vibration*, *371*, 132–149. ISSN 0022-460X.

Gassner, G., & Kopriva, D. A. (2011). A comparison of the dispersion and dissipation errors of Gauss and Gauss-Lobatto discontinuous Galerkin spectral element methods. *SIAM Journal of Scientific Computing*, *33*(5), 2560–2579. ISSN 1064-8275.

Haller, G. (2005). An objective definition of a vortex. *Journal of Fluid Mechanics*, *525*, 1–26. ISSN 1469-7645, 0022-1120.

Hindenlang, F. (2014). Mesh curving techniques for high order parallel simulations on unstructured meshes. Ph.D. thesis, University of Stuttgart.

Hindenlang, F., Gassner, G., Altmann, C., Beck, A., Staudenmaier, M., & Munz, C.-D. (2012). Explicit discontinuous Galerkin methods for unsteady problems. *Computers and Fluids*, *61*, 86–93. ISSN 0045-7930.

Hindenlang, F., Bolemann, T., & Munz, C.-D. (2015). Mesh curving techniques for high order discontinuous Galerkin simulations. In N. Kroll, C. Hirsch, F. Bassi, C. Johnston, & K. Hillewaert (Eds.), *IDIHOM: Industrialization of high-order methods - a top-down approach* (Vol. 128, pp. 133–152). Notes on numerical fluid mechanics and multidisciplinary design. New York: Springer International Publishing. doi:10.1007/978-3-319-12886-3_8. ISBN 978-3-319-12885-6 978-3-319-12886-3.

Howe, M. S. (2003). *Theory of vortex sound*. Cambridge: Cambridge University Press.

Hussaini, M. Y., Kopriva, D. A., Salas, M. D., & Zang, T. A. (1985). Spectral methods for the Euler equations. i - Fourier methods and shock capturing. *AIAA Journal*, *23*(1), 64–70. ISSN 0001-1452.

Jones, L., & Sandberg, R. (2010). Numerical investigation of tonal airfoil self-noise generated by an acoustic feedback-loop. In *16th AIAA/CEAS Aeroacoustics Conference*. American Institute of Aeronautics and Astronautics. doi:10.2514/6.2010-3701.

Jones, L. E., & Sandberg, R. D. (2011). Numerical analysis of tonal airfoil self-noise and acoustic feedback-loops. *Journal of Sound and Vibration*, *330*(25), 6137–6152. ISSN 0022-460X.

Khalighi, Y., Mani, A., Ham, F., & Moin, P. (2010). Prediction of sound generated by complex flows at low mach numbers. *AIAA Journal*, *48*(2), 306–316. ISSN 0001-1452.

Kingan, M. J., & Pearse, J. R. (2009). Laminar boundary layer instability noise produced by an aerofoil. *Journal of Sound and Vibration*, *322*(4), 808–828. ISSN 0022-460X.

Kirby, R. M., & Karniadakis, G. E. (2003). De-aliasing on non-uniform grids: Algorithms and applications. *Journal of Computational Physics*, *191*(1), 249–264. ISSN 0021-9991.

Kolmogorov, A. N. (1999). The local structure of turbulence in incompressible viscous fluid for very large Reynolds numbers. *Royal Society of London Proceedings Series A*, *434*, 9–13. doi:10.1098/rspa.1991.0075.

Kopriva, D. A. (2006). Metric identities and the discontinuous spectral element method on curvilinear meshes. *Journal of Scientific Computing*, *26*(3), 301. ISSN 0885-7474, 1573-7691.

Kopriva, D. A. (2009). *Implementing spectral methods for partial differential equations: Algorithms for scientists and engineers* (1st ed.). New York: Springer Publishing Company Incorporated. ISBN 9048122600, 9789048122608.

Kopriva, D. A., & Gassner, G. (2010). On the quadrature and weak form choices in collocation type discontinuous Galerkin spectral element methods. *Journal of Scientific Computing*, *44*(2), 136–155. ISSN 0885-7474, 1573-7691.

Lele, S. K. (1997). Computational aeroacoustics: A review. *AIAA Paper*, *18*, 1997.

Lesaint, P., & Raviart, P.-A. (1974). On a finite element method for solving the neutron transport equation. In C. A. deBoor (Ed.), *Mathematical aspects of finite elements in partial differential equations* (pp. 89–145). New York: Academic Press.

Lighthill, M. J. (1952). On sound generated aerodynamically. i. General theory. *Proceedings of the Royal Society of London A: Mathematical, Physical and Engineering Sciences*, *211*(1107), 564–587. ISSN 1364-5021, 1471-2946.

Lounsberry, T. H., Gleason, M. E., & Puskarz, M. M. (2007). Laminar flow whistle on a vehicle side mirror. In SAE Technical Paper. SAE International, 04.

Nash, E. C., Lowson, M. V., & McAlpine, A. (1999). Boundary-layer instability noise on aerofoils. *Journal of Fluid Mechanics*, *382*, 27–61. ISSN 1469-7645, 0022-1120.

Paterson, R. W., Vogt, P. G., Fink, M. R., & Munch, C. L. (1973). Vortex noise of isolated airfoils. *Journal of Aircraft*, *10*(5), 296–302. ISSN 0021-8669.

Plogmann, B., Herrig, A., & Wuerz, W. (2013). Experimental investigations of a trailing edge noise feedback mechanism on a NACA 0012 airfoil. *Experiments in Fluids*, *54*(5), 1480. ISSN 0723-4864, 1432-1114.

Pruett, C. D., Gatski, T. B., Grosch, C. E., & Thacker, W. D. (2003). The temporally filtered Navier-Stokes equations: Properties of the residual stress. *Physics of Fluids*, *15*(8), 2127–2140. ISSN 1070-6631.

Reed, W. H., & Hill, T. R. (1973). Triangular mesh methods for the neutron transport equation. Technical report LA-UR-73-479, Los Alamos Scientific Laboratory.

Shebalin, J. (1993). Pseudospectral simulation of compressible turbulence using logarithmic variables. In *11th Computational Fluid Dynamics Conference*. American Institute of Aeronautics and Astronautics.

Tam, C., & Webb, J. C. (1993). Dispersion-relation-preserving finite difference schemes for computational acoustics. *Journal of Computational Physics*, *107*(2), 262–281. ISSN 0021-9991.

Tam, C. K. W. (1974). Discrete tones of isolated airfoils. *Journal of the Acoustical Society of America*, *55*, 1173–1177.

Tam, C. K. W., & Hardin, J. C. (1997). Second computational aeroacoustics (CAA) workshop on benchmark problems. NASA Conference Publications.

Toro, E. F. (1999). *Riemann solvers and numerical methods for fluid dynamics*. New York: Springer.

Werner, M. (2017). Experimental study on tonal self-noise generated by aeroacoustic feedback on a side mirror. Ph.D. thesis, University of Stuttgart.

Werner, M. J., Würz, W., & Krämer, E. (2017a) Experimental investigation of an aeroacoustic feedback mechanism on a two-dimensional side mirror model. *Journal of Sound and Vibration*, *387*, 79–95. ISSN 0022-460X.

Werner, M. J., Würz, W., & Krämer, E. (2017b). Experimental investigation of the tonal self-noise emission of a vehicle side mirror. *Accepted for publication in AIAA Journal*.

Yokokawa, M., Itakura, K., Uno, A., Ishihara, T., & Kaneda, Y. (2002). 16.4-tflops direct numerical simulation of turbulence by a Fourier spectral method on the earth simulator. In *Supercomputing, ACM/IEEE 2002 Conference* (pp. 50–50).